JGR Oceans

RESEARCH ARTICLE
10.1029/2019JC014976

Special Section:
The Arctic: An AGU Joint Special Collection

Retrieval of Wintertime Sea Ice Production in Arctic Polynyas Using Thermal Infrared and Passive Microwave Remote Sensing Data

Andreas Preußer[1], Kay I. Ohshima[2,3], Katsushi Iwamoto[2,4,5], Sascha Willmes[1], and Günther Heinemann[1]

[1]Environmental Meteorology, University of Trier, Trier, Germany, [2]Institute of Low Temperature Science, Hokkaido University, Sapporo, Japan, [3]Arctic Research Center, Hokkaido University, Sapporo, Japan, [4]Arctic Environment Research Center, National Institute of Polar Research, Tachikawa, Japan, [5]Mombetsu, Japan

Key Points:
- Overall high agreement between independent MODIS and AMSR-E data sets on observed Arctic polynya characteristics
- High-resolution MODIS data set beneficial in narrow coastal areas and the evaluation of long-term trends in polynya area and ice production
- Analysis of 16 winter seasons reveals significantly increasing ice formation in polynyas along the Siberian coast

Correspondence to:
A. Preußer,
preusser@uni-trier.de

Citation:
Preußer, A., Ohshima, K. I., Iwamoto, K., Willmes, S., & Heinemann, G. (2019). Retrieval of wintertime sea ice production in Arctic polynyas using thermal infrared and passive microwave remote sensing data. *Journal of Geophysical Research: Oceans*, *124*, 5503–5528. https://doi.org/10.1029/2019JC014976

Received 28 JAN 2019
Accepted 10 JUL 2019
Accepted article online 20 JUL 2019
Published online 4 AUG 2019

Abstract Precise knowledge of wintertime sea ice production in Arctic polynyas is not only required to enhance our understanding of atmosphere-sea ice-ocean interactions but also to verify frequently utilized climate and ocean models. Here, a high-resolution (2-km) Moderate Resolution Imaging Spectroradiometer (MODIS) thermal infrared satellite data set featuring spatial and temporal characteristics of 17 Arctic polynya regions for the winter seasons 2002/2003 to 2017/2018 is directly compared to an akin low-resolution Advanced Microwave Scanning Radiometer-EOS (AMSR-E) passive microwave data set for 2002/2003 to 2010/2011. The MODIS data set is purely based on a 1-D energy-balance model, where thin-ice thicknesses ($\leq$ 20 cm) are directly derived from ice-surface temperature swath data and European Centre for Medium-Range Weather Forecasts Re-Analysis-Interim atmospheric reanalysis data on a quasi-daily basis. Thin-ice thicknesses in the AMSR-E data set are derived empirically. Important polynya properties such as areal extent and potential thermodynamic ice production can be estimated from both pan-Arctic data sets. Although independently derived, our results show that both data sets feature quite similar spatial and temporal variations of polynya area (POLA) and ice production (IP), which suggests a high reliability. The average POLA (average accumulated IP) for all Arctic polynyas combined derived from both MODIS and AMSR-E are 1.99×10^5 km^2 (1.34×10^3 km^3) and 2.29×10^5 km^2 (1.31×10^3 km^3), respectively. Narrow polynyas in areas such as the Canadian Arctic Archipelago are notably better resolved by MODIS. Analysis of 16 winter seasons provides an evaluation of long-term trends in POLA and IP, revealing the significant increase of ice formation in polynyas along the Siberian coast.

Plain Language Summary The term "polynya" essentially describes the appearance of "holes" in an otherwise closed sea ice cover, that are kept free of thick sea ice due to strong physical forcing mechanisms such as wind or warmer ocean temperatures. The size of such a polynya can sometimes exceed several tens of thousands of square kilometers, indicating a high physical and biological importance. The contrast between the relatively warm ocean and the cold atmosphere creates a flow of heat to the atmosphere that causes intense freezing at the ocean surface. Gaining a more detailed knowledge about the total amount of new sea ice that is formed in these polynyas during the Arctic winter is highly important to understand the large-scale characteristics of the Arctic sea ice cover. Using different kinds of satellite data, this study follows the aim to analyze the difference in Arctic-wide polynya monitoring between two independent and previously published data sets. Our results show that both data sets show highly similar estimations of polynya size and new sea ice production, with the overall Arctic-wide difference being in the range of 2–15%. The results of this study enhance the confidence when using the data sets for other applications and when analyzing long-term developments and trends of Arctic polynyas.

1. Introduction

One of the most characteristic features in the polar sea ice cover are polynyas. These recurrent areas of open water and thin ice appear throughout the freezing season, thereby modulating physical, biological, and chemical processes at the boundary between atmosphere and ocean on local to regional scales (Barber & Massom, 2007). In the Arctic shelf seas, the main mechanism for polynya openings are divergent ice motions

induced by wind stress (Smith et al., 1990) so that the timing, duration, and areal extent of a polynya usually features a large variability on multiple time scales (Morales-Maqueda et al., 2004). Contrary to sea ice leads, which show a rather nonstationary behavior on short time scales (Willmes & Heinemann, 2016), polynyas tend to appear on more or less confined (well-defined) locations, often connected to orographic or sea ice mechanic features such as fast-ice edges, ice bridges, ice shelves, or icebergs. Barber and Massom (2007) presented a thoroughly compiled inventory of prominent polynya locations on both hemispheres. However, some of the therein depicted polynyas underwent noticeable changes over the last decade in terms of, for example, polynya-opening frequencies and areal extent (Iwamoto et al., 2014; Preußer et al., 2015, 2016; Tamura & Ohshima, 2011, among others).

From an oceanographic and atmospheric perspective, surface energy fluxes and ice production (IP) rates are the most interesting quantities that can be derived for thin-ice areas (i.e., polynyas and leads) in the polar sea ice cover (Barber & Massom, 2007; Hollands & Dierking, 2016; Morales-Maqueda et al., 2004). Particularly during winter, the thin-ice cover promotes a large energy loss to the atmosphere that leads to strong IP and brine release in polynyas. Ultimately, this has direct implications for the lower atmospheric boundary layer as well as the ocean stratification and bottom water formation. In order to precisely detect, track, and quantify long-term dynamics of polynyas as well as linkages to other environmental components in the polar climate system, an accurate and regular monitoring of these and other thin-ice areas is necessary. For approximately 40 years, various studies showed that remote sensing approaches using passive microwave and thermal infrared data have proven to be valuable tools for this task. The resulting data can be utilized for verifying or augmenting (regional) climate and ocean models (Ebner et al., 2011, 2014; Gutjahr et al., 2016; Sansiviero et al., 2017, among others).

Thin-ice thicknesses (TIT) can be derived through algorithms that link brightness temperatures (T_B) from passive microwave instruments such as Special Sensor Microwave/Imager (SSM/I) and Advanced Microwave Scanning Radiometer-EOS (AMSR-E) to TIT derived from thermal infrared radiometers (e.g., Advanced Very High Resolution Radiometer or Moderate Resolution Imaging Spectroradiometer [MODIS]) in empirical approaches (Martin et al., 2004, 2005, and others). Based on this concept, Tamura and Ohshima (2011) developed a new algorithm for SSM/I data and used it to provide the first circumpolar mapping of polynya dynamics and IP in the Arctic on a relatively coarse 25×25-km^2 grid. Iwamoto et al. (2013) and Iwamoto et al. (2014, hereafter I14) improved on several aspects of the applied empirical approach, with the most obvious changes being an increased grid resolution of 6.25×6.25 km^2 through the use of AMSR-E data and increased capabilities to discriminate fast-ice and open water areas by introducing distinct masking procedures. Recent work by Nakata et al. (2019) includes further improvements to this particular approach to estimate TIT by first classifying polynya regions into zones of active frazil ice formation and thin solid ice and subsequently applying variable empirical relationships depending on these ice types. Nihashi et al. (2017) presented first results on transferring the empirical approach to derive TIT (and polynya IP) to Advanced Scanning Microwave Radiometer 2 (AMSR-2) data for four distinct polynya regions around Antarctica. As the time periods covered by AMSR-E and AMSR-2 are separated by 9 months, the resulting data gap has been closed by using data from the SSM/I-SSMIS satellite platforms that have been adjusted to the AMSR-E/2 retrievals. An equivalent AMSR-2 data set for the Arctic is not yet available. Other satellite-based active (i.e., Sythetic Aperature Radar) and passive microwave sensors, such as the European Space Agency's Sentinel-1 and Soil-Moisture-Ocean-Salinity (SMOS), respectively, have so far not been used for dedicated (pan-Arctic) polynya studies due to their comparatively low temporal/spatial resolutions.

The sole use of thermal infrared satellite data to analyze wintertime polynya (i.e., thin-ice and open water areas) dynamics has in the past been limited to case studies and/or single winter seasons (Adams et al., 2013; Aulicino et al., 2014; Drucker et al., 2003; Mäkynen & Karvonen, 2017; Willmes et al., 2010, 2011, and others), as the high amount of cloud cover in the polar regions and inherent problems with the use of thermal infrared (i.e., optical) data are difficult to overcome. Scott et al. (2014) presented a study on assessing the TIT for operational data assimilation using both MODIS thermal infrared data as well as AMSR-E passive microwave data along the Labrador Coast, northeastern Canada. With the use of a triple collocation method, they found that the error associated with ice thickness from AMSR-E was the lowest, and with ice thickness from MODIS it was the highest. However, their approach did not feature a dedicated cloud artifact screening or other procedures to minimize the error associated with clouds, as they were not trying to analyze persistent sea ice features but to derive near-seamless ice charts for assimilation purposes. By introducing additional cloud checks and different spatial and temporal interpolation schemes, the studies by

Table 1
Main Characteristics of the Two Published Satellite-Based Data Sets by Iwamoto et al. (2014) and Preußer et al. (2016) on Arctic Polynyas

Characteristics	AMSR-E (Iwamoto et al., 2014)	MODIS (MxD29 C5) (Preußer et al., 2016)
Sensor type	Passive microwave radiometer	Thermal infrared radiometer
Method for thin-ice retrieval	Empirical approach: AMSR-E T_B data linked to reference ice thicknesses from 1-D energy balance model	Direct application of a 1-D energy balance model (different parametrization than Iwamoto et al., 2014)
Analyzed time period	2002/2003 to 2010/2011 (September to May)	2002/2003 to 2014/2015 (November to March)
Grid resolution	6.25 km	2 km
Restrictions	Possible ambiguities from open water and fast ice	Only nighttime and clear-sky conditions
Cloud influence	Mostly negligible; longwave radiation terms in energy balance equation adjusted for varying degrees of cloud cover	Not negligible; spatial and temporal interpolation techniques applied

Note. The abbreviation "MxD29" denotes both MOD29 from the Terra satellite and MYD29 from the Aqua satellite. Note that the present study uses a MODIS data set that has been updated using MxD29 Collection 6 up to winter season 2017/2018. Further, it now spans a reduced winter period from December to March each year (see text). AMSR-E = Advanced Microwave Scanning Radiometer-EOS; MODIS = Moderate Resolution Imaging Spectroradiometer.

Paul, Willmes, Gutjahr, et al. (2015), Paul, Willmes, and Heinemann (2015), Preußer, Willmes, et al. (2015), and Preußer, Heinemann, et al. (2015) recently showed that it is feasible to use thermal infrared data for a wintertime polynya monitoring over long time periods. This led to the first high-resolution (~2-km) mapping of circumpolar polynya regions and IP in the Arctic using only MODIS thermal infrared data and European Center for Medium-Range Weather Forecasts (ECMWF) ERA-Interim atmospheric reanalysis data for the period from 2002 to 2015 by Preußer et al. (2016, hereafter P16).

Regarding long-term investigations of polynya dynamics in both the Arctic and Antarctic shelf seas, it is difficult to assess which kind of approach is better suited without conducting a direct intercomparison on both local and circumpolar scales. Hence, the main idea of this study is to perform such a direct intercomparison in order to get a better understanding of the overall differences, the benefits, and deficits of each approach, as well as to evaluate if a potential future synergy is a feasible goal. Ultimately, this comparison may add to an increased confidence when analyzing the changing characteristics of polynyas in the context of a warming Arctic. The main characteristics of the two studies (I14/P16) that led to the idea of this study are summarized in Table 1. It is obvious that both approaches follow in some aspects different concepts and both deal with a variety of sensor-specific advantages, ambiguities, and restrictions. In addition, varying temporal and spatial references (analyzed time periods and polynya regions) limit fair quantitative comparisons on the basis of published results, metrics, and spatial distributions. Consequently, this study is based on a common definition for Arctic polynya regions based on the spatial margins from P16 (Figure 1).

We organized the paper as follows. After a profound description of the used data sets and methods, the subsequent two chapters will elaborate on the outcome of this direct comparison as well as some of the required preconsiderations such as potential bias effects. Our results are then discussed in the context of other (remote sensing) studies on (Arctic) polynyas together with some final conclusions at the end of the paper.

2. Data and Methods

2.1. Data Overview: Remote Sensing and Atmospheric Reanalysis

Daily T_B data from the AMSR-E instrument on board the Aqua satellite platform are available from June 2002 to October 2011 (AMSR-E/Aqua Level 3 product; Cavalieri et al., 2004). Horizontally and vertically

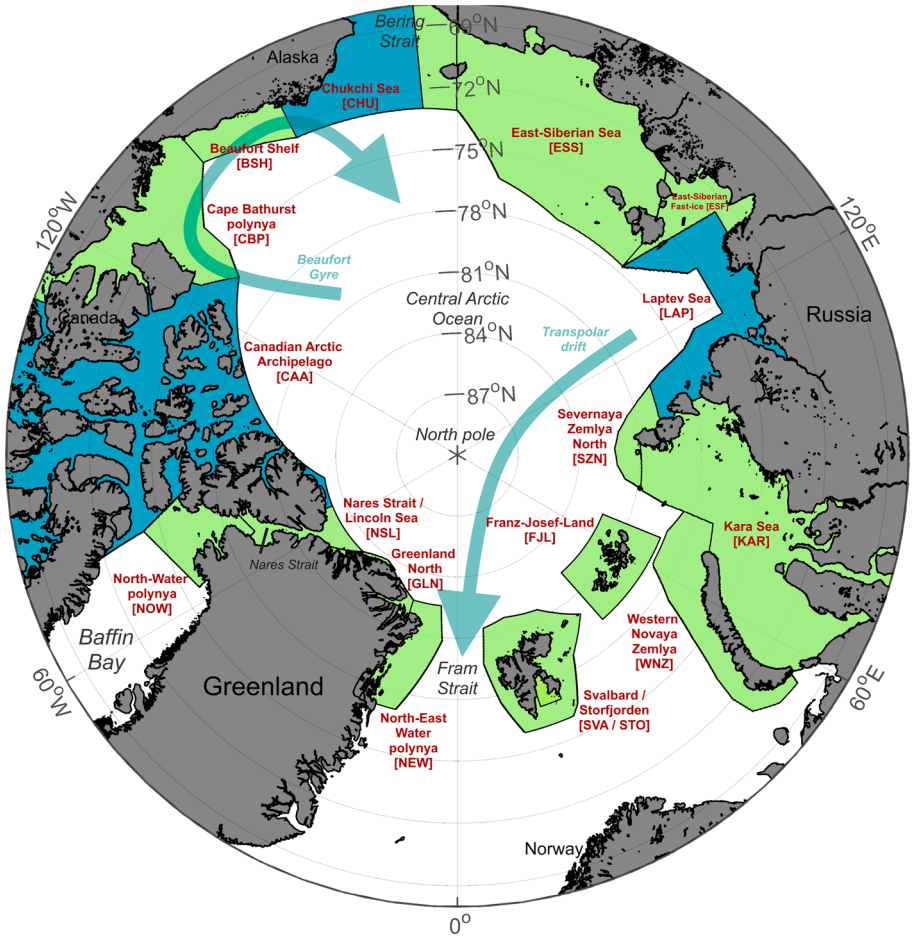

Figure 1. Spatial overview of all investigated areas of interest (i.e., polynya masks) located in the Arctic, enclosing the typical location of each polynya in wintertime. Blue areas denote areas that are being investigated in more detail in later chapters, while all other areas are colored in green. Arrows indicate the approximate drift pattern of sea ice in the Beaufort Gyre and Transpolar Drift region.

polarized T_B from the 89.0- and 36.0-GHz frequency channels are used at a spatial resolution of 6.25×6.25 km^2 and 12.5×12.5 km^2, respectively. These data are then used in an empirical approach combined with MODIS thermal infrared data to derive a so-called thermal ice thickness (Iwamoto et al., 2013; Iwamoto et al., 2014).

For the derivation of TIT, we now use the MxD29 (MxD: both MOD29 from Terra satellite and MYD29 from Aqua satellite) Collection 6 (C6) sea ice product (Hall et al., 2004; Riggs & Hall, 2015) derived from MODIS satellite data, which is considered to be an improvement compared to the Collection 5 (C5) data set used in P16. We incorporate data from both MODIS instruments on board the Terra and Aqua polar-orbiting satellite platforms, that is acquired over ocean areas north of 68°N. The product features swath data of ice surface temperatures (IST) with a spatial resolution of 1×1 km^2 at nadir and includes the MODIS cloud mask (MxD35 C6; Ackerman et al., 2010). Main changes compared to MxD29 C5 are an altered L1B calibration of the TIR channels to improve the accuracy of IST in very cold scenes, an update of the MODIS land/water mask that changed some coastline definitions (e.g., northern Greenland) as well as changes to the cloud mask, which now includes a new nighttime ocean test that improved on the detection of low level and cirrus clouds Riggs and Hall (2015). However, the overall accuracy of the MxD29 C6 IST remains at around 1 to 3 K (Hall et al., 2004; Riggs & Hall, 2015). The usage of MODIS C6 instead of C5 data has effects on some of the derived polynya statistics, and it will be shown later that some regions are more influenced by the introduced version changes than others.

All 17 polynya masks (reference areas; cf. Figure 1) from P16 are adapted for the 6.25-km passive microwave grid, and the winter period for all nine winters available in both data sets (2002/2003 to 2010/2011) is set to an overlapping time span from December to March. In contrast to previous studies, November data are excluded in the present study in order to focus on winter polynya dynamics only and reduce the effects of a late freeze-up in autumn. The latter has become increasingly frequent in recent years in the Barents, Kara, and Chukchi Seas (Stroeve et al., 2014, and others) and impacts the derived polynya statistics through a high fraction of thin sea ice with nonpolynya origin.

Regarding data from atmospheric reanalysis, both studies used the ECMWF ERA-Interim reanalysis at 0.75° (~80-km) horizontal resolution (Dee et al., 2011). Atmospheric variables that are being used in the heat flux calculations (see following section) by both P16 and I14 thereby include the 2-m temperature, 2-m dew point temperature, 10-m horizontal wind, the pressure at mean sea level, and (medium-level) cloud-cover information at a temporal resolution of 6 hr. In case of MODIS (P16), the reanalysis data are linearly interpolated to a 1-hr resolution. For the calculation of TIT, individual MODIS swaths are then linked to the closest time of the (interpolated) atmospheric fields from ERA-Interim. Finally, all ERA-Interim data fields are spatially interpolated and projected on the common higher resolution reference grid (2 km for MODIS and 6.25 km for AMSR-E).

It should be noted that for areas with small-scale topographic structures such as the Nares Strait the ERA-Interim data may not be realistic. For the area of the North Water polynya, the reanalysis largely underestimate the wind induced by the the gap flow through Smith Sound, which leads also to an underestimation of the turbulent fluxes at the surface (Moore & Våge, 2018; Heinemann, 2018). In order to account for the small-scale topographic structures in the Canadian and Greenland region, models with resolutions of at least 15 km are needed Gutjahr and Heinemann (2018).

2.2. MODIS TIT Retrieval and Composite Generation

Estimating the TIT from MODIS (MxD29 C6) IST data employs a 1-D energy-balance model (Adams et al., 2013; Preußer et al., 2016; Yu & Rothrock, 1996; Yu & Lindsay, 2003, among others), wherein the satellite data are combined with atmospheric reanalysis data to calculate the turbulent heat fluxes and the longwave radiative fluxes. These are then used to derive TIT up to 20 cm by assuming a balance between the atmospheric heat flux Q_{atm} (thus restricting to nighttime conditions) and the conductive heat flux through the ice, Q_{ice}:

$$Q_{\mathrm{atm}} = Q_0 - H_0 - E_0 \tag{1}$$

$$Q_{\mathrm{ice}} = \kappa_{\mathrm{ice}} \cdot \frac{(T_s - T_f)}{h_{i,\mathrm{th}}} \tag{2}$$

where Q_0 is the radiation balance, H_0 and E_0 are the turbulent fluxes of sensible heat and latent heat, respectively, κ_{ice} is the thermal conductivity of sea ice, T_s is the surface temperature, T_f the freezing point of sea water, and $h_{i,\mathrm{th}}$ is the ice thickness (th = "thermal"). Ice thicknesses are only calculated when Q_{atm} is negative (energy loss of the surface). Because of difficulties with the parametrization of shortwave radiation terms Adams et al. (2013) and in order to avoid dealing with snow and ice albedo effects, only nighttime scenes are incorporated into the calculations (pixel-wise check for solar zenith angles $\leq 0°$). We assume the newly formed ice in a polynya (≤ 20 cm) to be free of snow, with a linear temperature profile between the surface (IST) and the lower boundary of the ice (constant; freezing point of sea water). The turbulent fluxes of sensible and latent heat were calculated by an iterative bulk approach (Launiainen & Vihma, 1990) based on the Monin-Obukhov similarity theory. Following the initial assumption that Q_{atm} equals Q_{ice}, $h_{i,\mathrm{th}}$ is calculated from

$$h_{i,\mathrm{th}} = \kappa_{\mathrm{ice}} \cdot \frac{(T_{\mathrm{s}} - T_{\mathrm{f}})}{Q_{\mathrm{atm}}} \tag{3}$$

Here, we support our analysis with the sole usage of ERA-Interim reanalysis data (Dee et al., 2011), although the use of different atmospheric products imposes a certain spread on derived polynya statistics (Adams et al., 2013) and, as a consequence, a range of uncertainty. One restriction to this particular method is the limitation to clear-sky conditions during polar night conditions, which imposes distinct challenges on the satellite-data processing chain and requires a set of assumptions and corrections in order to be used in a

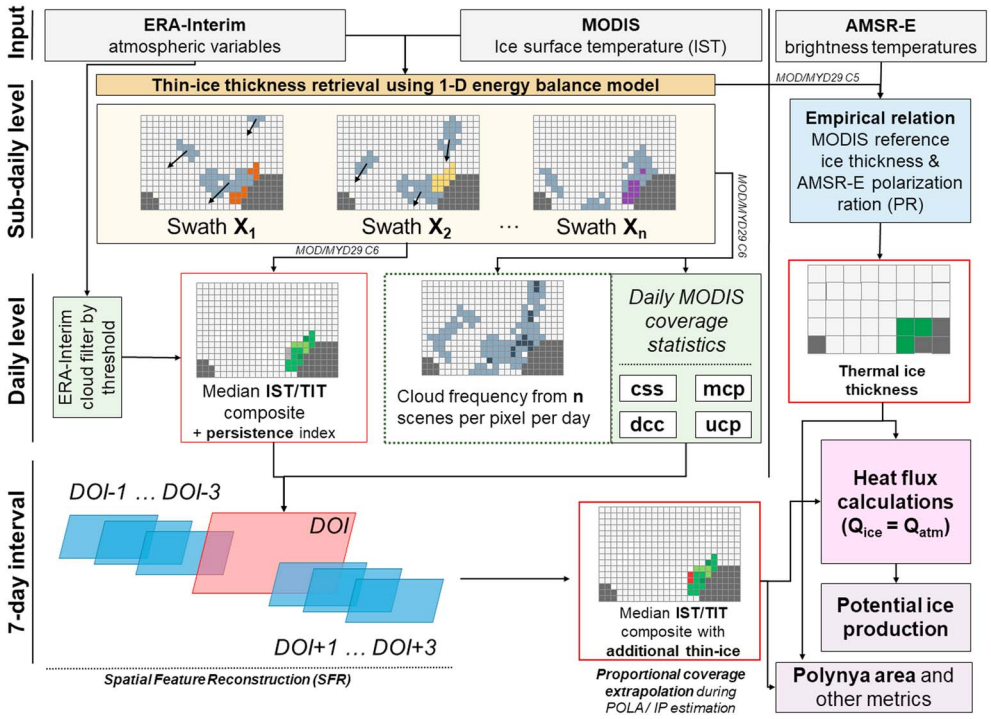

Figure 2. Overview on the processing schemes to derive thin-ice thicknesses of both (left) Preußer et al. (2016) and (right) Iwamoto et al. (2014). The abbreviations "IST," "TIT," and "PR" denote the ice-surface temperature, thin-/thermal-ice thickness, and polarization ratio, respectively. Q_{atm} and Q_{ice} are the atmospheric heat flux and conductive heat flux through the ice. Other abbreviations include the following: day of interest (DOI), confident clear-sky (css), mixed-cover pixels (mcp), definitively cloud-covered (dcc), and uncovered pixel (ucp). ERA = European Centre for Medium-Range Weather Forecasts Re-Analysis; MODIS = Moderate Resolution Imaging Spectroradiometer; AMSR-E = Advanced Microwave Scanning Radiometer-EOS; POLA = polynya area; IP = ice production.

long-term investigation. One main aspect of this approach is the calculation of daily IST and TIT median composites from single swath-data, which increases the amount of potentially usable IST information for an individual pixel substantially due to the high number of daily overpasses by both MODIS sensors at polar latitudes. ERA-Interim medium cloud-cover information is used in addition to mask out potentially remaining cloud signatures in the composites that are not detected by the MODIS cloud mask (MxD35; Ackerman et al., 2010), which is integrated in the MxD29 IST product. Besides, a (thin-ice) persistence threshold of 50% is applied to filter out short-lived and uncertain thin-ice pixels on a daily basis (Preußer et al., 2015; Paul, Willmes, and Heinemann 2015). The processing chain (left side in Figure 2) further includes the application of a spatial feature reconstruction algorithm (Paul, Willmes, Gutjahr, et al., 2015) as well as a proportional scaling approach for the remaining minor data gaps within polynya-mask margins (Preußer, Willmes, et al., 2015). Both procedures involve spatial and/or temporal interpolation techniques to compensate for cloud gaps in the daily TIT composites, which then feature a substantially enhanced spatial coverage (Table 2; cf. also Paul, Willmes, Gutjahr, et al., 2015; Preußer et al., 2015).

Based on these daily corrected composites and using the method described, for example, in Preußer et al. (2015), IP rates (IPRs) are calculated for each pixel with an ice thickness $\leq$ 0.2 m, that is, the commonly referenced ice-thickness range for polynya areas (Adams et al., 2013; Willmes et al., 2010). This is within the range of grey-white ice (WMO, 2014). In a sensitivity analysis of this method (without the spatial feature reconstruction), Adams et al. (2013) stated an uncertainty for the ice-thickness retrieval of $\pm$1.0, $\pm$2.1, and $\pm$5.3 cm for thin-ice classes of 0–5, 5–10, and 10–20 cm, respectively.

While I14 follow a similar approach to derive reference ice thicknesses (equation (3)) from MODIS IST for their empirical approach (following section; right side in Figure 2), there are distinct differences in the individual parametrization of the latent and sensible heat fluxes and the estimation of the downward longwave radiation flux (Ohshima et al., 2003). However, the resulting effect on the estimated ice thickness below 20 cm is overall quite small. Please refer to Appendix A for more details.

Table 2
The Interannual (2002/2003 to 2017/2018; December to March) Average Daily MODIS Coverage (Decimal Cover Fraction Ranging From 0 to 1 With Their Respective Standard Deviations) for Each Polynya Region Before (COV2) and After (COV4) Application of the Spatial Feature Reconstruction (SFR)

Region	COV2 (ccs, HQ mcp)	COV4 (ccs, HQ mcp, SFR)
Beaufort Shelf (BSH)	0.85 ± 0.03	0.99 ± 0.00
Canadian Arctic Archipelago (CAA)	0.87 ± 0.02	0.99 ± 0.00
Cape Bathurst (CBP)	0.85 ± 0.02	0.98 ± 0.00
Chukchi Sea (CHU)	0.83 ± 0.04	0.98 ± 0.02
East Siberian Fast-Ice (ESF)	0.83 ± 0.03	0.99 ± 0.01
East Siberian Sea (ESS)	0.85 ± 0.02	0.98 ± 0.01
Franz-Josef-Land (FJL)	0.82 ± 0.03	0.98 ± 0.01
Greenland North (GLN)	0.85 ± 0.04	0.98 ± 0.01
Kara Sea (KAR)	0.78 ± 0.04	0.97 ± 0.02
Laptev Sea (LAP)	0.84 ± 0.03	0.99 ± 0.01
North East Water (NEW)	0.84 ± 0.04	0.99 ± 0.01
North Water (NOW)	0.88 ± 0.04	0.99 ± 0.01
Nares Strait/Lincoln Sea (NSL)	0.88 ± 0.03	0.99 ± 0.01
Storfjorden (STO)	0.82 ± 0.05	0.98 ± 0.02
Svalbard Archipelago (SVA+STO)	0.68 ± 0.09	0.89 ± 0.06
Severnaya Zemlya North (SZN)	0.84 ± 0.05	0.99 ± 0.01
Western Novaya Zemlya (WNZ)	0.59 ± 0.09	0.82 ± 0.07
Total	0.82 ± 0.04	0.97 ± 0.02

Note. The abbreviation "ccs" denotes confident clear-sky coverage, while "HQ mcp" is high-quality mixed-cover pixels where either MODIS or ERA-Interim medium cloud cover features cloud signals in the daily composites. An overview on all applied predefined polynya masks is given in Figure 1. MODIS = Moderate Resolution Imaging Spectroradiometer; ERA = European Centre for Medium-Range Weather Forecasts Re-Analysis

2.3. Empirical TIT Retrieval Using AMSR-E

The calculation of TIT using passive microwave brightness temperatures (SSM/I-SSMIS, AMSR-E, and AMSR2) commonly follows the principle of empirically linking polarization ratios (PR) of T_B, which are influenced by the circumstance that the surface salinity is correlated with ice thickness (Naoki et al., 2008), to reference TIT derived by thermal infrared sensors such as Advanced Very High Resolution Radiometer or MODIS (Cavalieri, 1994; Iwamoto et al., 2013, 2014; Tamura et al., 2007, 2008; Tamura & Ohshima, 2011; Willmes et al., 2010, among others). As PR values at a given frequency decrease as the sea ice thickens, the relation to the ice thickness can be expressed through linear or exponential regressions (Tamura & Ohshima, 2011). Other similar approaches are based on a simple ratio between the horizontally and vertically polarized T_B at 36 and 37 GHz (Martin et al., 2004, 2005; Willmes et al., 2010) and T_B at 89 GHz (Willmes et al., 2010), or combinations of PR, simple ratios, or gradient ratios (GR) of T_B (Aulicino et al., 2014; Naoki et al., 2008).

In this study, we adapt the TIT algorithm developed for AMSR-E by Iwamoto et al. (2014) and used their data set. The data set is based on earlier work by Iwamoto et al. (2013), who derived an exponential relationship between AMSR-E PR and MODIS TIT for the Chukchi Sea. Iwamoto et al. (2014) then presented the applicability to the North Water polynya and Laptev Sea, thereby concluding on the validity for the entire Arctic Ocean. The procedure to derive the thermal infrared-based MODIS reference data closely follows the one described in the previous section (Preußer et al., 2016).

The following relationships between PR and ice thickness ($h_{i,\mathrm{th}}$) up to 0.2 m were obtained by Iwamoto et al. (2013) to infer the so-called thermal (i.e., microwave) ice thickness:

$$h_{i,mw} = \exp[1/(218 \times \mathrm{PR}_{89} - 3.0)] - 1.03 \quad \text{for} \quad \mathrm{PR}_{89} \geq 0.05 \tag{4}$$

$$h_{i,mw} = \exp[1/(206 \times PR_{36} - 5.4)] - 1.02 \quad \text{for} \quad PR_{89} < 0.05 \tag{5}$$

Here, the subscripts "89" and "36" indicate the microwave frequencies (in *GHz*) of the observed brightness temperatures T_B, $h_{i,mw}$ is the ice thickness (mw = "microwave") inferred from the empirical relation. Iwamoto et al. (2013) state a bias of ±1.0 cm and a standard deviation of 3.7–5.6 cm for their ice-thickness estimation in the Chukchi Sea. The ice thickness by the algorithm tends to exhibit false thin ice signals over the landfast ice areas. Thus, a fast ice mask was developed in I14, which eliminated such false signals by using the gradient ratio between the brightness temperatures of 89 and 36 GHz. I14 also proposed the combined use of PR_{89} and PR_{36}, PR_{89} being first used for thicknesses of 0–0.1 m (corresponding to $PR_{89} \geq 0.05$) and then PR_{36} for thicknesses of 0.1–0.2 m ($PR_{89} < 0.05$). In addition, as the 89-GHz data in the microwave range are to some degree affected by water vapor and cloud liquid water in the atmosphere, a dedicated masking procedure using 36-GHz data is required to account for disturbing effects. Hence, all pixels that satisfy equation (6) are considered inhibit signatures from water vapor or cloud liquid water and are regarded as erroneous pixels.

$$PR_{89} < 3.2 \times (PR_{36})^2 - 0.077 \times (PR_{36}) + 0.0066 \tag{6}$$

In their pan-Arctic study, Iwamoto et al. (2014) closed resulting data gaps by replacing pixels discarded by equation (6) with the ice thickness derived from PR_{36}. In the main winter period with high polynya activity from November to April, these pixels account to about 3% of all thin-ice pixels. Equations (4) and (5) are used for calculating thin ice thickness, with open water pixels being excluded in advance. The detection of open water follows a procedure/criteria that depends on the different frequencies: First, all pixels with ice thicknesses from PR_{36} that are below a sea ice concentration threshold of 30% are treated as open water. After that, an additional PR_{89} open water mask is applied where all pixels with $PR_{89} > 0.11$ are regarded as open water (Iwamoto et al., 2013; Iwamoto et al., 2014).

2.4. Derivation of Potential Thermodynamic IP in Polynyas

The calculation of potential thermodynamic IP requires an accurate characterization of the distribution of thin-ice and open water within the margins of a detected polynya. The previous two sections showed how this can be done using either thermal infrared (i.e., optical) sensors or passive microwave radiometers. The term "thermodynamic" implies that calculated estimates represent the amount of ice that would be formed under ideal thermodynamic conditions, that is, with no dynamic contribution to ice growth such as ridging and rafting, and assuming a uniform layer of ice within a grid cell. As in equation (1) the oceanic heat flux from below is omitted (which would lower the amount of heat loss to the atmosphere), the term "potential" is used. A oceanic contribution to the surface energy balance could reduce the thermodynamic ice growth by around 23–27% in case of the NOW polynya (Tamura & Ohshima, 2011; Iwamoto et al., 2014) due to a potential influence of the West Greenland Current in northern Baffin Bay (Steffen, 1985; Yao & Tang, 2003). Further, for certain areas of the Chukchi Sea (Hirano et al., 2016; Hirano et al., 2018) and the Canadian Arctic Archipelago (CAA) (Hannah et al., 2009; Melling et al., 2015) it is either known or assumed that there is an oceanic influence on wintertime polynya dynamics.

The usage of a fixed thickness-threshold for polynyas (cf. section 2.2) certainly has an influence on the derivation of thermodynamic IP within the its margins, so that for instance a change of the upper thickness-threshold from 20 to 30 cm would cause an increase by about 5% to 16% in annually accumulated IP. However, due to this rather minor effect and the circumstance of increasing ice-thickness uncertainties beyond 20 cm, the limitation to the 0- to 20-cm thickness range can be justified.

A common approach to calculate IPRs is using information on the ice thickness (distribution) in combination with meteorological data from atmospheric reanalysis data sets, such as the ECMWF ERA-Interim (Dee et al., 2011) or National Center for Environmental Prediction NCEP2 (Kanamitsu et al., 2002) reanalysis (see section 2.1). Despite coarse spatial resolutions and ultimately large uncertainties of these data sets, a wide range of earlier remote sensing studies (Iwamoto et al., 2014; Martin et al., 2005; Renfrew et al., 2002; Tamura et al., 2007; Tamura & Ohshima, 2011; Willmes et al., 2011, among others) and model studies (Bauer et al., 2013; Ebner et al., 2011; Jardon et al., 2014, among others) followed this approach. The present study also uses coarse resolution atmospheric reanalysis data, as this is currently one of the few viable options when investigating large and remote spatial domains with a very low amount of in situ data.

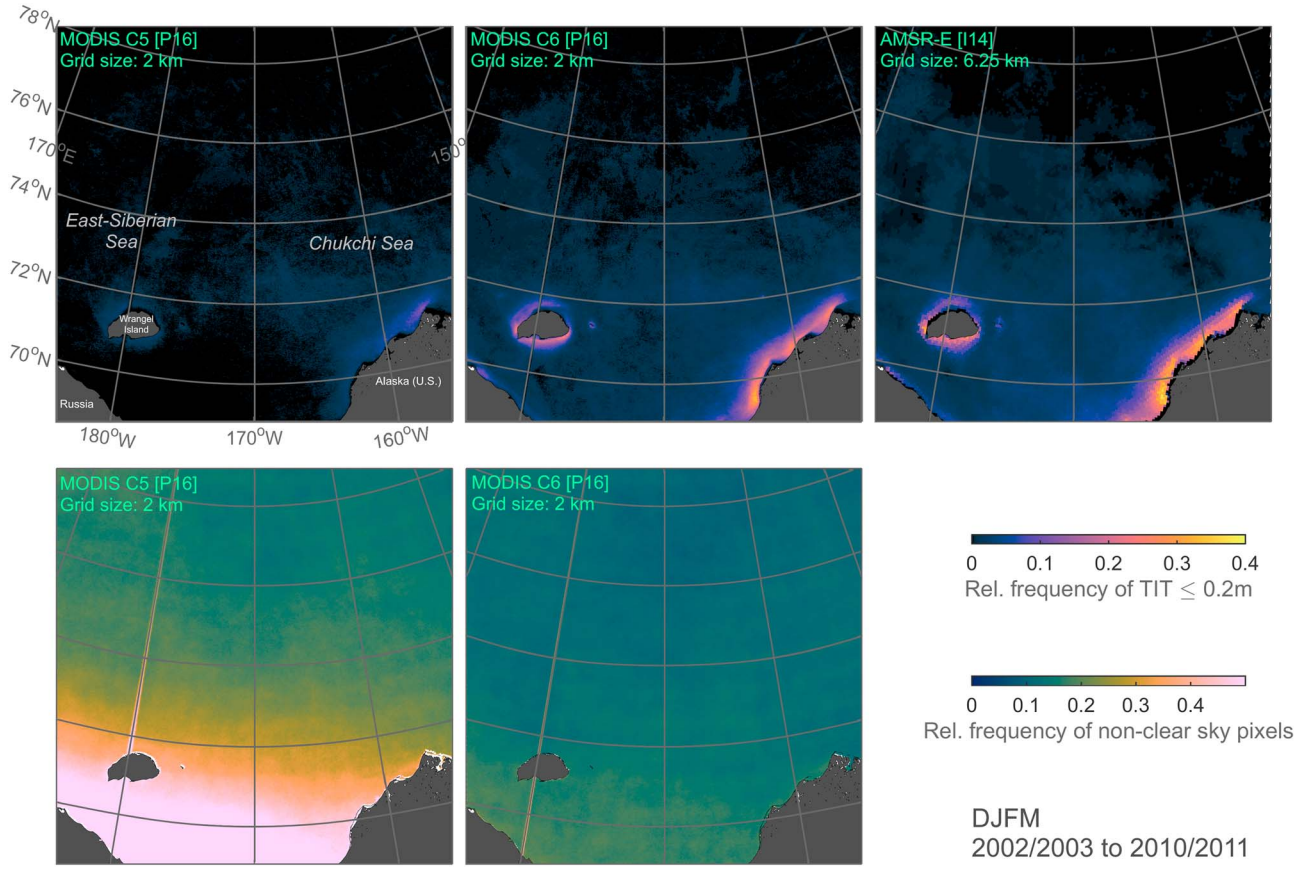

Figure 3. (top row) Wintertime (December to March) frequencies of thin-ice thicknesses (TIT) ≤ 0.2 m in the Pacific sector of the Arctic between 2002/2003 and 2010/2011. This represents the overlapping period between MODIS data (P16; MxD29 C5 and C6) and AMSR-E data (I14). Frequencies are calculated per pixel as the fraction of days with a TIT ≤ 0.2 m relative to this 9-year period. (bottom row) Frequencies of non–clear sky (i.e., low-quality mixed cover and cloud-covered) MODIS pixels corresponding to the upper MODIS C5/C6 panels, relative to the same 9-year period from 2002/2003 to 2010/2011. MODIS = Moderate Resolution Imaging Spectroradiometer; AMSR-E = Advanced Microwave Scanning Radiometer-EOS; DJFM = December–March.

In general, IPRs are derived by assuming that the entire heat loss at the ice surface to the overlying atmosphere contributes to new ice formation (Tamura et al., 2007, 2008; Willmes et al., 2011).

$$\frac{\partial h}{\partial t} = \frac{-\bar{Q}_{\text{ice}}}{\rho_{\text{ice}} \cdot L_f} \tag{7}$$

Equation (7) provides the IPR $\frac{\partial h}{\partial t}$, with ρ_{ice} being the density of the ice ($\rho_{\text{ice}} = 910\,\text{kg/m}^3$; Timco & Frederking, 1996) and L_f being the latent heat of fusion of sea ice ($L_f = 0.334$ MJ/kg; Tamura & Ohshima, 2011). The daily conductive heat flux through the ice $\bar{Q}_{\text{ice}}$ is known from equation (1), that is, the result of atmospheric heat flux calculations under the condition that Q_{atm} equals Q_{ice}. However, the usage of fixed values for ρ_{ice} and L_f is of course a simplification that introduces an additional error source arising from spatially and temporally varying conditions for ice formation. In case of AMSR-E ice thickness data, the surface temperature T_s is essential to calculate Q_{ice}. T_s can be iteratively determined under the assumption of $Q_{\text{atm}} = Q_{\text{ice}}$ from equations (1) and (2), where the radiation terms are calculated by empirical formulations given by Cavalieri and Martin (1994) and Maykut and Church (1973), respectively, and the turbulent heat fluxes are estimated from the bulk methods using the IST and atmospheric data. The in situ validation of IPRs in thin-ice areas is a highly difficult task, especially during wintertime. Hence, IP derived by the above described approach should currently be regarded as a potential upper limit for thermodynamically induced ice growth.

3. Precomparison Considerations

3.1. Update on MODIS-Derived Polynya Characteristics Using MxD29 C6

As mentioned in section 2.1, the update of the MODIS (MxD29) input data set of ISTs from C5 to C6 has a spatially varying influence on derived polynya statistics, including the estimation of potential thermodynamic

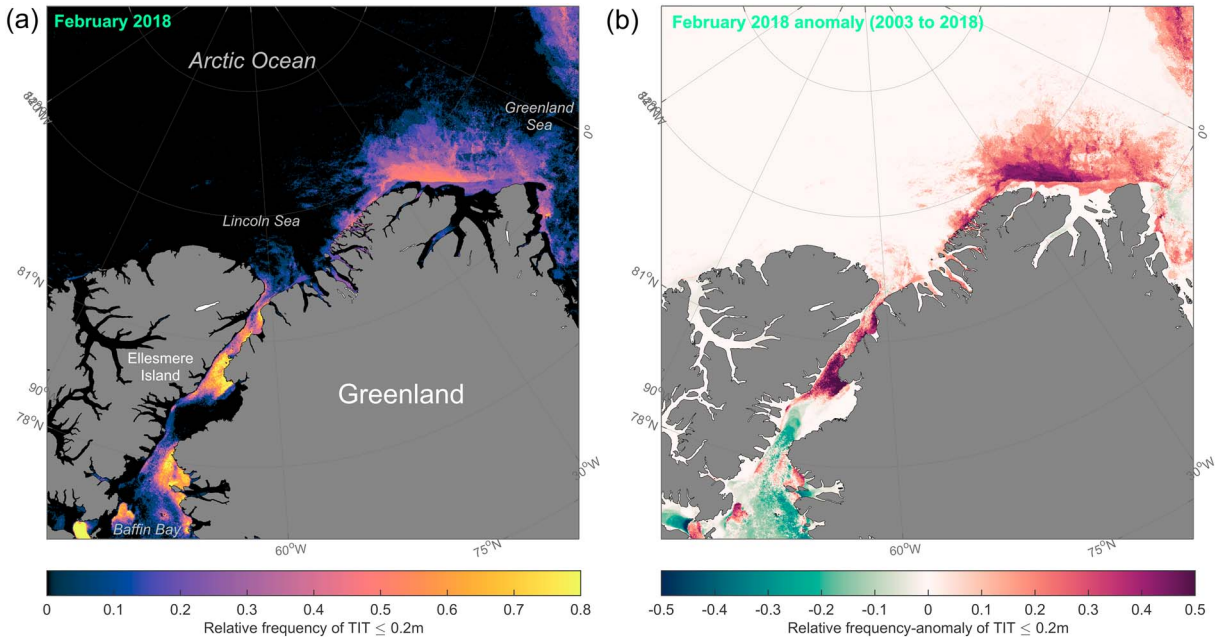

Figure 4. Spatial distribution of relative thin-ice frequencies around northern Greenland in February 2018 (a), based on daily ice thicknesses derived from MOD/MYD29 (C6) ice-surface temperatures and ERA-Interim reanalysis data (cf. respective section). Note the exceptionally large polynya area north of Greenland as a quite rare feature in this region during winter. Other geographical features are indicated by their respective names. (b) The February 2018 anomalies relative to the long-term (2003 to 2018) distribution of thin-ice frequencies, where reddish and blue-greenish colors indicate positive and negative anomalies, respectively. ERA = European Centre for Medium-Range Weather Forecasts Re-Analysis.

sea IP. The most noticeable change in C6 is a modified procedure to handle clouds, which apparently results in a less conservative cloud masking that allows for more satellite pixels being considered cloud-free in a certain time interval. In order to illustrate this effect, Figure 3 first shows a side-by-side comparison of the long-term (2002 to 2011; December–March [DJFM]) average frequency of occurrence of TIT less than 20 cm (relative to the 9-year period; top row). These were derived from MODIS C5, MODIS C6, and AMSR-E data (left to right in Figure 3). While the pan-Arctic context of these thin-ice frequencies will be discussed later, the Chukchi Sea/Pacific sector of the Arctic is chosen on purpose here, as this area featured more frequent cloud occurrences in past MODIS polynya studies (Preußer et al., 2016). This can be seen in the bottom row of Figure 3, which shows the relative frequency of non–clear sky pixels in both the MODIS C5 and MODIS C6 data set, defined as the sum of all definitely cloud-covered and low-quality mixed-cover pixels relative to the 9-year period. The MODIS C5 data set shows non–clear sky (i.e., most probably cloud-covered) frequencies exceeding 40% to 50% in the southern Chukchi Sea toward Bering Strait. This changes to largely reduced frequencies in the MODIS C6 equivalent, with values around 20% to 30% in the respective regions. This has an obvious effect on the derived TIT distributions, where the MODIS C6 and AMSR-E versions are closely matching both in a spatial and quantitative sense, unlike the MODIS C5 and AMSR-E distributions.

The new MODIS C6-based record of daily TIT data in the Arctic features 16 winter seasons up to 2017/2018, which extends the data record by 3 years compared to the study by Preußer et al. (2016). Therefore, it includes an interesting polynya-feature appearing in February 2018 at the northern coast of Greenland, where open-water and thin-ice conditions prevailed over a period of about 15 days. This is rather unusual in this particular part of the Arctic Ocean/Greenland Sea as the area usually contains some of the thickest multiyear ice fractions in the whole Arctic. Figure 4a shows a distribution of thin-ice frequencies (relative to the total number of days in February) around northern Greenland, together with the anomalies of those frequencies related to an average February in the 2003 to 2018 period (Figure 4b). In the core polynya areas along the (fast-ice extended) shoreline at the northern tip of Greenland, frequencies are exceeding 50% (>14 days), while areas at the margins (approximately maximum extent) prevailed about 2 to 7 days (including very narrow shore leads at the western margin). Almost the complete polynya area shows positive anomalies which further points to the unusual nature of this polynya. Compared to other known high productive areas such as the North Water polynya or the southern Lincoln Sea, our estimates of accumulated IP in these highly

Journal of Geophysical Research: Oceans

10.1029/2019JC014976

Table 3
Average Polynya Area (POLA) in Square Kilometers in Each Polynya Region Between 2002/2003 and 2017/2018 (Second and Third Columns) as Well as 2002/2003 and 2010/2011 (Remaining Columns)

	MODIS (2002/2003 vs. 2017/2018)		MODIS (2002/2003 vs. 2010/2011)		AMSR-E (2002/2003 vs. 2010/2011)		DIFF: MODIS – AMSR-E (2002/2003 vs. 2010/2011)	
Region	Average POLA (10^3 km^2)	Trend POLA (10^3 km^2 [%]/year)	Average POLA (10^3 km^2)	Trend POLA (10^3 km^2 [%]/year)	Average POLA (10^3 km^2)	Trend POLA (10^3 km^2 [%]/year)	Absolute (10^3 km^2)	Percentage (%)
Beaufort Shelf (BSH)	2.5 ± 2.1	−0.1 (−4)	3.0 ± 2.5	−0.2 (−7)	2.4 ± 2.2	−0.02 (−1)	0.6	−20
Canadian Arctic Archipelago (CAA)	17.5 ± 4.8	0.3 (1)	17.2 ± 5.6	*1.4* (8)	9.4 ± 2.3	0.3 (4)	7.9	−46
Cape Bathurst (CBP)	7.5 ± 4.4	0.2 (3)	7.0 ± 3.9	−0.2 (−3)	5.7 ± 3.1	−0.2 (−3)	1.3	−19
Chukchi Sea (CHU)	13.8 ± 6.0	0.5 (3)	11.8 ± 5.7	−0.4 (−4)	12.8 ± 4.1	−0.2 (−1)	−1.0	8
East Siberian Fast Ice (ESF)	0.6 ± 0.4	0.03 (5)	0.4 ± 0.2	0.01 (3)	0.6 ± 0.2	0.04 (8)	−0.1	30
East Siberian Sea (ESS)	8.9 ± 5.2	0.2 (2)	8.7 ± 5.4	0.7 (8)	7.8 ± 6.3	0.6 (8)	0.9	−11
Franz Josef Land (FJL)	13.4 ± 5.6	**0.7** (5)	11.1 ± 4.6	*1.0* (9)	15.4 ± 5.8	0.8 (5)	−4.4	40
Greenland North (GLN)	1.0 ± 0.7	0.04 (4)	0.9 ± 0.8	0.03 (3)	0.5 ± 0.3	0.05 (10)	0.4	−41
Kara Sea (KAR)	31.2 ± 16.6	*1.7* (5)	24.9 ± 11.8	2.1 (8)	44.1 ± 17.5	*3.8* (9)	−19.2	77
Laptev Sea (LAP)	10.6 ± 4.2	**0.5** (4)	8.8 ± 2.6	*0.6* (7)	9.0 ± 3.8	0.6 (7)	−0.2	2
Northeast Water (NEW)	2.5 ± 0.9	0.0 (0)	2.6 ± 0.7	0.02 (1)	7.1 ± 4.7	−0.2 (−3)	−4.5	173
North Water (NOW)	26.2 ± 7.2	0.2 (1)	24.8 ± 6.1	0.2 (1)	22.1 ± 6.1	0.02 (0)	2.7	−11
Nares Strait–Lincoln Sea (NSL)	3.9 ± 2.7	0.03 (1)	4.5 ± 2.8	0.5 (10)	2.9 ± 1.7	0.2 (6)	1.6	−36
Storfjorden (STO)	3.5 ± 1.3	0.1 (3)	3.0 ± 1.1	0.2 (5)	4.8 ± 1.0	0.1 (3)	−1.8	60
Svalbard Archipelago (SVA+STO)	29.9 ± 5.1	0.2 (1)	28.8 ± 4.3	0.1 (0)	44.3 ± 3.0	−0.5 (−1)	−15.4	54
Severnaya Zemlya North (SZN)	2.5 ± 1.5	***0.2*** (8)	1.7 ± 0.8	**0.2** (12)	2.1 ± 1.1	0.1 (7)	−0.4	21
Western Novaya Zemlya (WNZ)	37.8 ± 12.2	−1.0 (−3)	42.7 ± 13.2	1.6 (4)	43.0 ± 10.5	1.6 (4)	−0.3	1
Total	209.9 ± 34.6	**3.7** (2)	199.0 ± 33.6	*7.5* (4)	229.1 ± 25.6	**7.2** (3)	−30.1	15

Note. Aside from being based on the available winter period from December to March, it is separated between estimates from MODIS (C6) and AMSR-E (Iwamoto et al., 2014). All values are derived from daily MODIS TIT composites/daily AMSR-E TIT charts after application of the predefined polynya masks (Figure 1). Absolute and relative annual trends (in square kilometers and percent) are additionally given in each column, where italic, bold, and bold-italic numbers denote statistical significance (two-sided *t* test) at the 90%, 95%, and 99% levels, respectively. MODIS = Moderate Resolution Imaging Spectroradiometer; AMSR-E = Advanced Microwave Scanning Radiometer-EOS; TIT = thin-ice thickness.

frequent thin-ice areas north of Greenland are rather low with about 1–2 m per winter at maximum (omitting a potential oceanic influence on polynya formation through relatively warm Atlantic water masses in Greenland Sea). However, as the largest proportion of these accumulated rates is originating from this single unusual polynya event, the values are still fairly impressive.

In the first columns of Tables 3 and 4, we present the update on derived polynya metrics (polynya area (POLA)/potential thermodynamic IP) from MODIS C6 data for the extended period from winters 2002/2003 to 2017/2018 (DJFM). The average total IP in all Arctic polynyas now sums up to 1,370 ± 229 km^3 per winter (cf. Table 4), which is certainly less than the previously estimated 1,811 km^3 Preußer et al. (2016) using MODIS C5 data up to the winter of 2014/2015 (November to March). This is a combined effect of leaving out the month of November (including freeze-up effects, especially in Kara Sea), extending the averaging interval by three winter seasons as well as the data version change. In order to separate the latter effect more clearly, we performed a direct comparison of MODIS C5 and C6 metrics for the overlapping period 2002/2003 to 2014/2015 (DJFM). It reveals an average difference in POLA and IP (all regions combined) of about 12,241 km^2 (+6.3%) and 70 km^3 (+5.4%), respectively. This offset originates solely from the changing data version and its inherent changes in cloud detection, coastline definitions, and IST calibration (Riggs & Hall, 2015). While this difference in derived IP is overall rather small, it can be as high as an increase by 64.5 km^3 (+482%) in case of the Chukchi Sea (CHU) and 28.9 km^3 (+233%) in case of the East Siberian Sea (ESS). Negative differences in IP are of minor magnitude overall and occur for instance north of Severnaya Zemlya (SZN; −6.3%) and west of Novaya Zemlya (WNZ; −7.4%). Overall, we consider the slight change in derived polynya statistics by using MODIS (MxD29) C6 data to be more realistic.

3.2. Clear-Sky Bias Evaluation and the Effect of Spatial Interpolation

In addition to the attempt to exclude cloud cover to the highest degree possible, the exclusive use of clear-sky MODIS imagery in the thermal infrared approach introduces a potential overestimation of the heat loss to the atmosphere on a subdaily and daily level. Since low-level clouds reduce the net radiative loss by about 50 W/m^2 in polar regions (Heinemann & Rose, 1990; König-Langlo & Augstein, 1994), the restriction to cloud-free conditions in the daily composites (subdaily time scale) results in a positive bias in IP, which has been estimated to be less than 0.4 m per winter (Preußer et al., 2016).

Furthermore, the restriction to clear-sky MODIS data in the Spatial Feature Reconstruction (SFR; Paul, Willmes, Gutjahr, et al., 2015) interpolation approach theoretically leads to a positive bias on a day-to-day time scale. The SFR algorithm has been developed to increase the information about otherwise cloud-covered areas in the daily MODIS TIT composites and has been successfully applied in both Arctic (Preußer et al., 2015, 2016) and Antarctic (Paul, Willmes, Gutjahr, et al., 2015; Paul, Willmes, and Heinemann, 2015) regions. It follows the principle that locations of cloud-induced gaps are compared with the corresponding ice thicknesses of the surrounding 6 days (for more details, please refer to the referenced studies). Thereby, a probability of thin-ice occurrence is derived using a weighted composite of the days surrounding an initial day of interest (DOI). In case of a sufficiently high probability, new polynya pixels are assigned and artificial ISTs and TIT can be calculated using a weighted average of the same surrounding 6 days (Paul, Willmes, Gutjahr, et al., 2015). The SFR approach is generally able to adequately reconstruct polynya pixels, given a sufficient satellite coverage surrounding the DOI. Problems can occur in areas with higher cloud frequencies (i.e., more persistent cloud cover), as the risk of low probability values that are unable to pass the set threshold in the 7-day sliding window is increased.

More cloud-insensitive passive microwave data from AMSR-E (I14) can be utilized to investigate potential effects of (spatial) interpolation. In order to evaluate if a varying degree of cloud cover (derived from MODIS cloud information/mixed-cover pixels) has an effect on the calculated IP from AMSR-E passive microwave data, Figure 5a first shows a time series (2002/2003 to 2010/2011, DJFM each winter) of IPR anomalies, normalized by their annual standard deviation. It is separated between (more) cloudy (50% to 100% cloudy; light orange) and more clear-sky (0% to 50% cloudy; dark orange) days by applying a MODIS mixed-cover pixel threshold on the AMSR-E IPR time series for a given winter at one pixel-location in the Chukchi Sea (71.24°N, 157.65°W, Fukamachi et al., 2017). Similar time series are given in Figures 5b and 5c for the 10-m wind speed and 2-m temperature, respectively, taken from the ERA-Interim atmospheric reanalysis. It shows that under more cloudy conditions, the average normalized IPR anomalies are for all but one winter season (2009/2010) lower than those under more clear-sky conditions and mostly negative (equivalent to an average anomaly of −0.7 cm/day), which indicates a tendency to lower heat fluxes (probably due to enhanced

Journal of Geophysical Research: Oceans

10.1029/2019JC014976

Table 4
Average Accumulated Ice Production (IP) in Cubic Kilometers in Each Polynya Region Between 2002/2003 and 2017/2018 (Second and Third Columns) as Well as 2002/2003 and 2010/2011 (Remaining Columns)

	MODIS (2002/2003 vs. 2017/2018)		MODIS (2002/2003 vs. 2010/2011)		AMSR-E (2002/2003 vs. 2010/2011)		DIFF: MODIS – AMSR-E (2002/2003 vs. 2010/2011)	
Region	Accumulated IP (km^3)	Trend IP (km^3 [%]/year)	Accumulated IP (km^3)	Trend IP (km^3 [%]/year)	Accumulated IP (km^3)	Trend IP (km^3 [%]/year)	Absolute (km^3)	Percentage (%)
Beaufort Shelf (BSH)	16 ± 14	−0.9 (−6)	20 ± 17	−1.6 (−8)	15 ± 12	−0.6 (−4)	6	−27
Canadian Arctic Archipelago (CAA)	129 ± 36	2.1 (2)	126 ± 40	*8.9* (7)	77 ± 16	1.6 (2)	49	−39
Cape Bathurst (CBP)	46 ± 26	1.4 (3)	43 ± 22	−1.0 (−2)	36 ± 18	−0.3 (−1)	6	−15
Chukchi Sea (CHU)	85 ± 34	1.9 (2)	74 ± 35	−3.7 (−5)	76 ± 25	−3.9 (−5)	−3	4
East Siberian Fast Ice (ESF)	4 ± 3	0.2 (5)	3 ± 1	0.1 (3)	4 ± 2	0.4 (9)	−1	40
East Siberian Sea (ESS)	51 ± 25	1.2 (2)	50 ± 24	3.3 (7)	42 ± 22	2.3 (5)	8	−15
Franz Josef Land (FJL)	86 ± 33	**3.6** (4)	76 ± 29	*6.9* (9)	89 ± 20	3.8 (4)	−13	18
Greenland North (GLN)	7 ± 6	0.2 (3)	7 ± 6	0.2 (3)	4 ± 3	0.4 (12)	3	−47
Kara Sea (KAR)	181 ± 94	**10.2** (6)	146 ± 63	12.4 (9)	207 ± 80	*17.7* (9)	−61	42
Laptev Sea (LAP)	70 ± 28	**3.0** (4)	58 ± 17	**4.4** (7)	64 ± 24	4.0 (6)	−6	10
Northeast Water (NEW)	16 ± 6	−0.3 (−2)	16 ± 5	−0.2 (−1)	42 ± 28	−0.9 (−2)	−26	156
North Water (NOW)	196 ± 58	1.6 (1)	186 ± 52	0.7 (0)	165 ± 44	−1.2 (−1)	21	−11
Nares Strait–Lincoln Sea (NSL)	29 ± 20	0.1 (0)	33 ± 21	3.0 (9)	25 ± 15	1.0 (4)	8	−25
Storfjorden (STO)	18 ± 6	0.5 (3)	16 ± 5	0.9 (6)	21 ± 3	0.5 (2)	−5	32
Svalbard Archipelago (SVA+STO)	168 ± 28	−1.4 (−1)	175 ± 20	−1.0 (−1)	200 ± 34	−7.1 (−4)	−24	14
Severnaya Zemlya North (SZN)	18 ± 10	***1.4*** (8)	13 ± 6	*1.5* (12)	15 ± 7	1.3 (9)	−2	16
Western Novaya Zemlya (WNZ)	266 ± 103	−7.7 (−3)	311 ± 112	13.4 (4)	250 ± 62	9.6 (4)	60	−19
Total	1370 ± 229	16.7 (1)	1337 ± 227	47.4 (4)	1312 ± 110	**28.1** (2)	25	−2

Note. Aside from being based on the available winter period from December to March, it is separated between estimates from MODIS (C6) and AMSR-E (Iwamoto et al., 2014). All values are derived from daily MODIS TIT composites/daily AMSR-E TIT charts after application of the predefined polynya masks (Figure 1). Absolute and relative annual trends (in cubic kilometers and percent) are additionally given in each column, where italic, bold, and bold-italic numbers denote statistical significance (two-sided *t* test) at the 90%, 95%, and 99% levels, respectively. MODIS = Moderate Resolution Imaging Spectroradiometer; AMSR-E = Advanced Microwave Scanning Radiometer-EOS; TIT = thin-ice thickness.

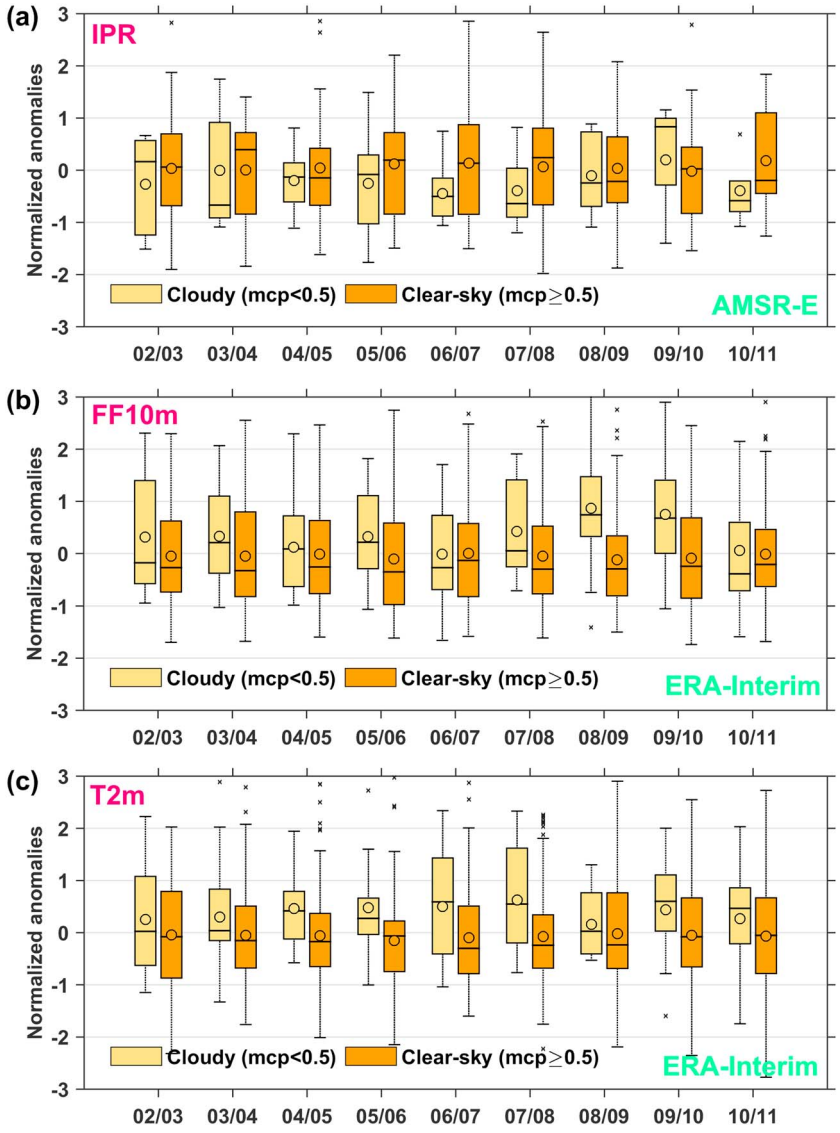

Figure 5. Normalized daily anomalies for different MODIS cloud-fraction classes for ice production rates (IPR) from AMSR-E (a), as well as for atmospheric variables from ERA-Interim reanalysis (b: 10-m wind speed; c: 2-m temperature) at the scale of a single AMSR-E pixel (here Chukchi Sea polynya at 71.24°N, 157.65°W). Time series show box plots for the overlapping MODIS/AMSR-E time period from 2002/2003 to 2010/2011 (December–March). Data for more cloudy (MODIS mixed-cover pixel [mcp] < 0.5; light orange) and more clear-sky (MODIS mcp ≥ 0.5; dark orange) conditions are shown. In each box plot, the circle denotes to the mean value for each distribution. Black bars indicate the median within the 25th and 75th percentiles (interquartile range; colored boxes). The whisker length has a default value of 1.5 times the interquartile range, and outliers are marked as black crosses. MODIS = Moderate Resolution Imaging Spectroradiometer; AMSR-E = Advanced Microwave Scanning Radiometer-EOS; ERA = European Centre for Medium-Range Weather Forecasts Re-Analysis; FF10m = 10-m wind speed; T2m = 2-m temperature.

downward long wave radiation). On the other hand, the average normalized IPR anomalies under more clear-sky conditions show no clear signature and vary around 0 (distance to the wintertime mean value in terms of standard deviations). This is similar for the atmospheric variables under more clear-sky conditions, while their more cloudy counterparts indicate on average higher wind speeds (equivalent average anomaly ~1 m/s) and increased 2-m temperatures (equivalent average anomaly ~2.4 K). Overall, while an effect through cloud cover on the daily IPR from AMSR-E can be inferred from Figure 5, it is apparently rather low with less than one standard deviation difference to the wintertime average IPR. Hence, we assume that the influence of a potential (positive) clear-sky bias in MODIS-based IP estimates is also rather small overall.

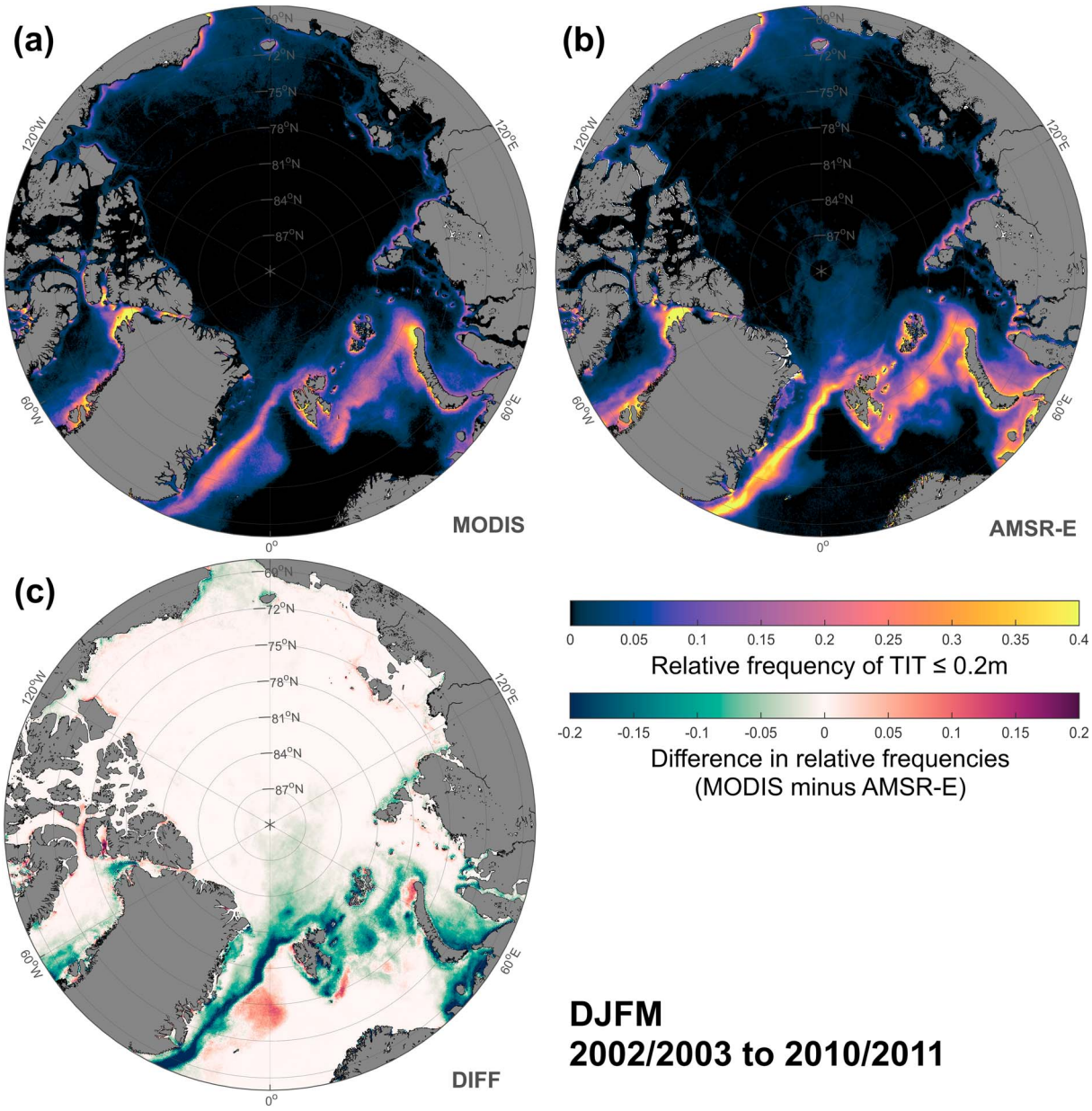

Figure 6. Wintertime (DJFM) frequencies of TIT ≤ 0.2 m in the Arctic between winters 2002/2003 and 2010/2011 for (a) MODIS (P16) and (b) AMSR-E (I14). Frequencies are calculated per pixel as the fraction of days with a TIT ≤ 0.2 m relative to the 9-year overlapping period. (c) The difference in relative frequencies between MODIS and AMSR-E, where negative values (blue-greenish colors) and positive values (red to violet colors) represent higher thin-ice frequencies for AMSR-E and MODIS, respectively. Note that the high-resolution MODIS data have been projected to the 6.25-km grid for this comparison. TIT = thin-ice thickness; MODIS = Moderate Resolution Imaging Spectroradiometer; AMSR-E = Advanced Microwave Scanning Radiometer-EOS; DJFM = December–March.

In a recent study, Nielsen-Englyst et al. (2018) investigated the relationship between high latitude snow and ice skin temperatures (including sea ice) and the 2-m air temperatures in the Arctic using data from 20 different in situ sites between 1997 and 2017. Therein, they also had a closer look at a potential clear-sky bias of satellite measurements of the IST by comparing clear-sky with all-sky in situ measurements over certain averaging intervals, including a 24-hr interval that compares well to the time interval by P16 when calculating daily median IST/TIT composites. They find that the averaged clear-sky bias of the IST during winter (December to February) is about −0.42 K for all considered sea ice stations. This represents a value that lies within the range of the indicated MODIS IST accuracy of 1–3 K (Hall et al., 2004; Riggs & Hall, 2015). Hence, the resulting effect of the bias indicated by Nielsen-Englyst et al. (2018) on TIT should not

exceed the statistical uncertainty of MODIS TIT (±4.7 cm for TIT ≤ 20 cm), as the uncertainty range of IST has been considered in the sensitivity analysis of TIT by Adams et al. (2013).

4. Long-Term Comparison of Thin-Ice Frequencies and IP

The previous two sections served the purpose to introduce, highlight, and elaborate more on some important differences and methodical challenges of both the passive microwave data set from AMSR-E as well as the thermal infrared data set from MODIS. All this was done to set the following long-term comparison (overlapping 9-year period) in the proper context regarding bias effects or data version changes. Relating back to Figure 3, pan-Arctic overviews with average wintertime (December to March) frequencies of TIT ≤ 0.2 m between 2002/2003 and 2010/2011 are shown in Figures 6a and 6b to give a first large-scale impression on typical polynya (i.e., thin-ice areas) locations in each data set. Overall, both MODIS and AMSR-E show a consistent pattern of high TIT frequencies (about ≥ 0.1, so more than 12 days per winter) almost throughout the whole Arctic, implying that the core regions of high polynya activity are well detected, independent of the difference in spatial resolution. In order to highlight the existing differences more clearly, Figure 6c shows the difference in wintertime thin-ice appearances, where greenish-blue and red colors denote to more thin-ice detected from AMSR-E and MODIS, respectively. Obviously, green-blueish colors are dominating in the Atlantic sector of the Arctic basin (marginal ice zone [MIZ]) as well as in some parts of Baffin Bay (particularly at the southern exit of Nares Strait and over the North Water polynya) and the Kara Sea. On the other hand, MODIS captures more thin ice (red to violet colors) in the narrow fjords throughout the CAA (+0.1 to +0.25 or more, equal to about 12 to 30 days per winter), in the northern Nares Strait, and around (northern) Greenland (about 0.15 or 18 days per winter), as well as the narrow flaw lead polynyas in the East Siberian, Laptev, and Kara Seas (about 0.05 to 0.15, or 6 to 18 days per winter). Note that thin-ice signals from the MIZ around the southern Fram Strait and Barents Sea (both at around 74°N) are mostly induced by artifacts from sea ice fracturing and feature ambiguities from variable ocean heat fluxes. Hence, those regions are not considered for quantitative analysis and excluded by applying polynya masks (Figure 1).

An extensive overview on derived polynya areas (POLA) for all considered polynya regions in the Arctic is given in Table 3. In its first column, the table features estimates for the complete 16-year long MODIS record of TIT from 2002/2003 to 2017/2018 (DJFM). The remaining columns show first the same MODIS-based estimates for a different averaging interval (2002/2003 to 2010/2011, DJFM), together with the corresponding AMSR-E estimates (2002/2003 to 2010/2011, DJFM) and a column with the resulting differences (absolute/percent). Absolute and relative trends are additionally indicated, despite the circumstance that the overlapping MODIS/AMSR-E investigation period until 2011 is relatively short and therefore highly sensitive to larger variances. An equivalent overview on derived IP estimates is presented in Table 4. It becomes obvious that the POLA/IP trends derived for the 16-year long time series are more significant for many regions, especially those regions being located around the Siberian shelf in the eastern Arctic. These include Franz-Josef-Land (FJL), the Laptev (LAP), and Kara (KAR) Seas, and the area north of Severnaya Zemlya (SZN). The latter features by far the most significant ($p \leq 0.01$) positive trends in POLA and IP with an increase of around 8% per year (2002/2003 to 2017/2018). In order to illustrate appearing trends on a spatial level, an updated map (2002/2003 to 2017/2018) of the trends in potential thermodynamic IP from MODIS can be seen in Figure 7. Again, the Siberian sector of the Arctic sticks out quite prominently, with the largest (significant) trends appearing along the coasts of the Laptev and Kara Seas. The only other regions with similar significance (Figure 7b) are found north of Devon Island (Canadian Arctic) and around northern Barents Sea, with the latter being mostly separated from coastal polynya regions and hence presumably more related to lead openings (Willmes & Heinemann, 2016) and/or MIZ dynamics. Preußer et al. (2016) already suggested some of the driving processes behind the increase in polynya frequencies and IP, such as a connection to the likewise increasing ice area export from the Siberian shelf, which itself is supposedly related to a generally thinner/younger and hence more mobile and fragile sea ice cover. Moreover, Krumpen et al. (2019) recently investigated changing characteristics of the long-range transport of sea ice and ice-rafted matter (IRM), both formed on the Siberian shelves, in the Transpolar Drift. They point out the theory that increasing IP (observed in our study and Preußer et al., 2016) could enhance the entrainment of IRM into newly formed sea ice and therefore increase the deposition along the Transpolar Drift during summer melt, with further consequences for primary production and biodiversity in the Arctic Ocean. As a result, changes in wintertime polynya dynamics on the Siberian shelves could have far-reaching consequences on the Arctic climate and ecosystem. Interestingly, the magnitude of calculated short-term trends does often not match

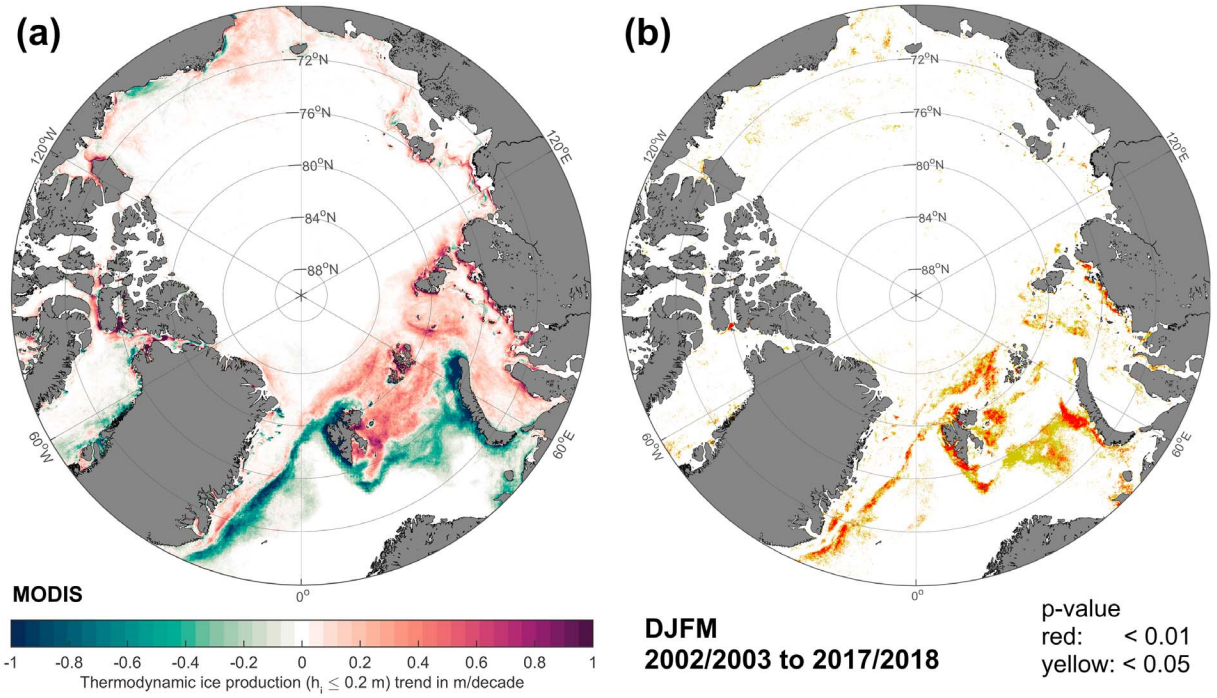

Figure 7. (a) Decadal trends (in meters per decade) of the potential thermodynamic ice production (for TIT ≤ 0.2 m) in the Arctic between December and March, north of 68°N. Trends are calculated by applying a linear regression to the annual accumulated IP per pixel for the period 2002/2003 to 2017/2018. Areas with statistical significance (based on a two-sided *t* test) at the 95% and 99% levels are depicted in panel (b). TIT = thin-ice thickness; IP = ice production; MODIS = Moderate Resolution Imaging Spectroradiometer; DJFM = December–March.

up between MODIS and AMSR-E, while on the other hand the tendency for positive/negative developments agrees better. For the overlapping period from 2002/2003 to 2010/2011, it shows that the average POLA (average accumulated IP) for all Arctic polynyas combined is 1.99×10^5 km^2 (1.34×10^3 km^3) in case of MODIS and 2.29×10^5 km^2 (1.31×10^3 km^3) for AMSR-E. Both average POLA and IP (total values) from MODIS are increased when extending the averaging interval to 2017/2018. Overall, the differences between MODIS and AMSR-E are quite small with about 15% in terms of POLA (mainly originating from Kara Sea) and −2% in terms of IP. On a regional level however, relative differences be as large as 156% (IP) to 173% (POLA) in case of the North East Water polynya.

In order to investigate some polynya regions in a bit more detail, the following three subsections will present regional close-ups of derived polynya metrics from both MODIS and AMSR-E. After the Laptev Sea flaw polynyas in the eastern Arctic, the other two sections will lead over to the western Arctic with larger polynyas in the Chukchi Sea and various scattered small polynyas in the Canadian Arctic.

4.1. Laptev Sea Flaw Polynyas

The Laptev Sea flaw lead polynyas, regularly forming due to off-shore components of the average wind-patterns along the fast-ice edge on the Siberian shelf (between approximately 70°N and 100°E, Figure 1), have been subject to many studies in the past (Bauer et al., 2013; Bareiss & Görgen, 2005; Dmitrenko et al., 2005, 2009; Ernsdorf et al., 2011; Gutjahr et al., 2016; Iwamoto et al., 2014; Martin & Cavalieri, 1989; Willmes et al., 2011;Tamura & Ohshima, 2011, and others). Most of these listed studies were aimed toward the characterization of polynya dynamics, water mass transformations, and sea ice formation in general, as those processes are all related to the circumstance that the Laptev Sea serves as one of the major source areas for sea ice export into the Transpolar Drift system (Dethleff et al., 1998; Krumpen et al., 2013; Itkin & Krumpen, 2017), with potential implications for the Arctic sea ice budget in general. As such, it is a highly relevant area to check both the MODIS and AMSR-E polynya metrics for consistency in that region, both in terms of spatial distribution of polynya appearances and in a quantitative sense.

Figure 8 shows spatial overviews of the average accumulated IP (in meters per winter; upper panels for AMSR-E and MODIS), a time series of the wintertime average polynya area (in square kilometers; lower left panel) and a time series of the accumulated total volume of IP (in cubic kilometers/winter; lower right

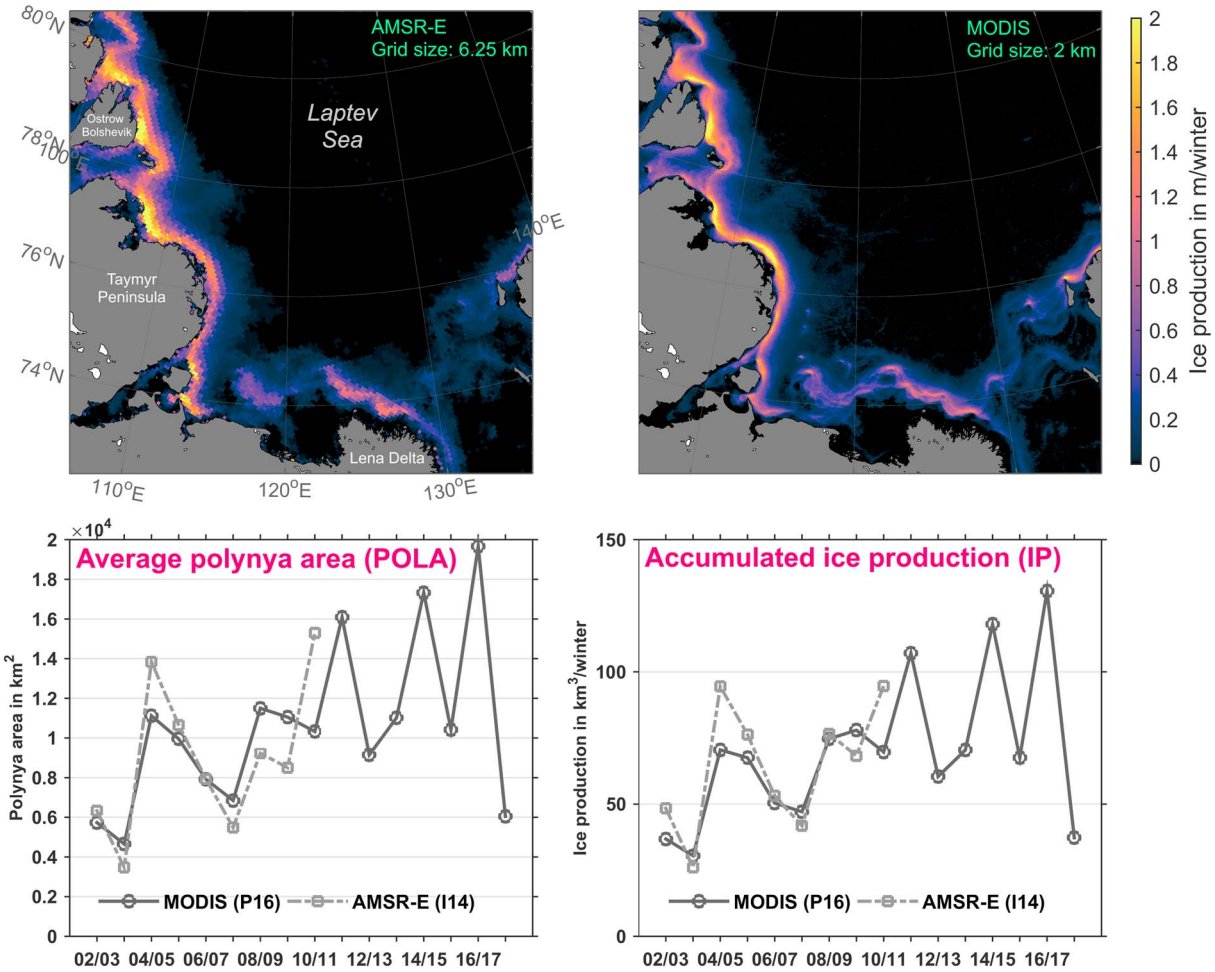

Figure 8. Comparison of Laptev Sea polynya characteristics between the cloud-corrected MODIS data set (P16) and the AMSR-E data set (I14). The two upper panels show spatial distributions of the average (2002/2003 to 2010/2011) accumulated ice production (meters per winter) during winter (December to March) for each sensor. The lower left and right panels illustrate a time series of the annual average polynya area (POLA; TIT ≤ 0.2 m) in square kilometers and the annual accumulated ice production (IP) in cubic kilometers, respectively, from 2002/2003 to 2017/2018. Both sensor systems (MODIS/AMSR-E) are compared, where dark and light gray lines denote MODIS (P16) and AMSR-E (I14), respectively. MODIS = Moderate Resolution Imaging Spectroradiometer; AMSR-E = Advanced Microwave Scanning Radiometer-EOS; TIT = thin-ice thickness.

panel). In case of the Laptev Sea, an overall quite close agreement both on a spatial and quantitative level can be noted. A larger band of polynyas with high IP values along the western coast of the Laptev Sea seems to be captured more or less equally well by both AMSR-E and MODIS, with slight differences in the locations of top-level IP around the Taymyr peninsula. In the (south)eastern Laptev Sea, IP is estimated higher from MODIS, as the increased spatial resolution is able to detect frequently appearing small flaw leads in proximity of the large fast-ice area, which develops in the course of each winter season. Overall, average polynya area and IP values in the Laptev Sea are very similar (POLA with 2% difference, IP with 10% difference), and annual values are in some years higher for MODIS, in other years for AMSR-E. The general trend in polynya area and IP is significantly positive for the MODIS estimates, independent of the considered time period. This is not the case for AMSR-E, while still being positive. As implied before (Figure 7 and Tables 3 and 4), increasing POLA and IP are also observed for adjacent polynya-regions such as SZN or Franz-Josef-Land, often connected to increasingly frequent polynya appearances.

4.2. Chukchi Sea Polynyas

Similar to the Laptev Sea, the Chukchi Sea has been subject to a huge number of in situ, remote sensing and modeling studies related to sea ice and dense-water formation (Cavalieri & Martin, 1994; Fukamachi et al., 2017; Hirano et al., 2016, 2018; Iwamoto et al., 2013, 2014; Martin et al., 2004, 2005; Tamura & Ohshima, 2011; Weingartner et al., 1998; Winsor & Björk, 2000; Winsor & Chapman, 2002, among

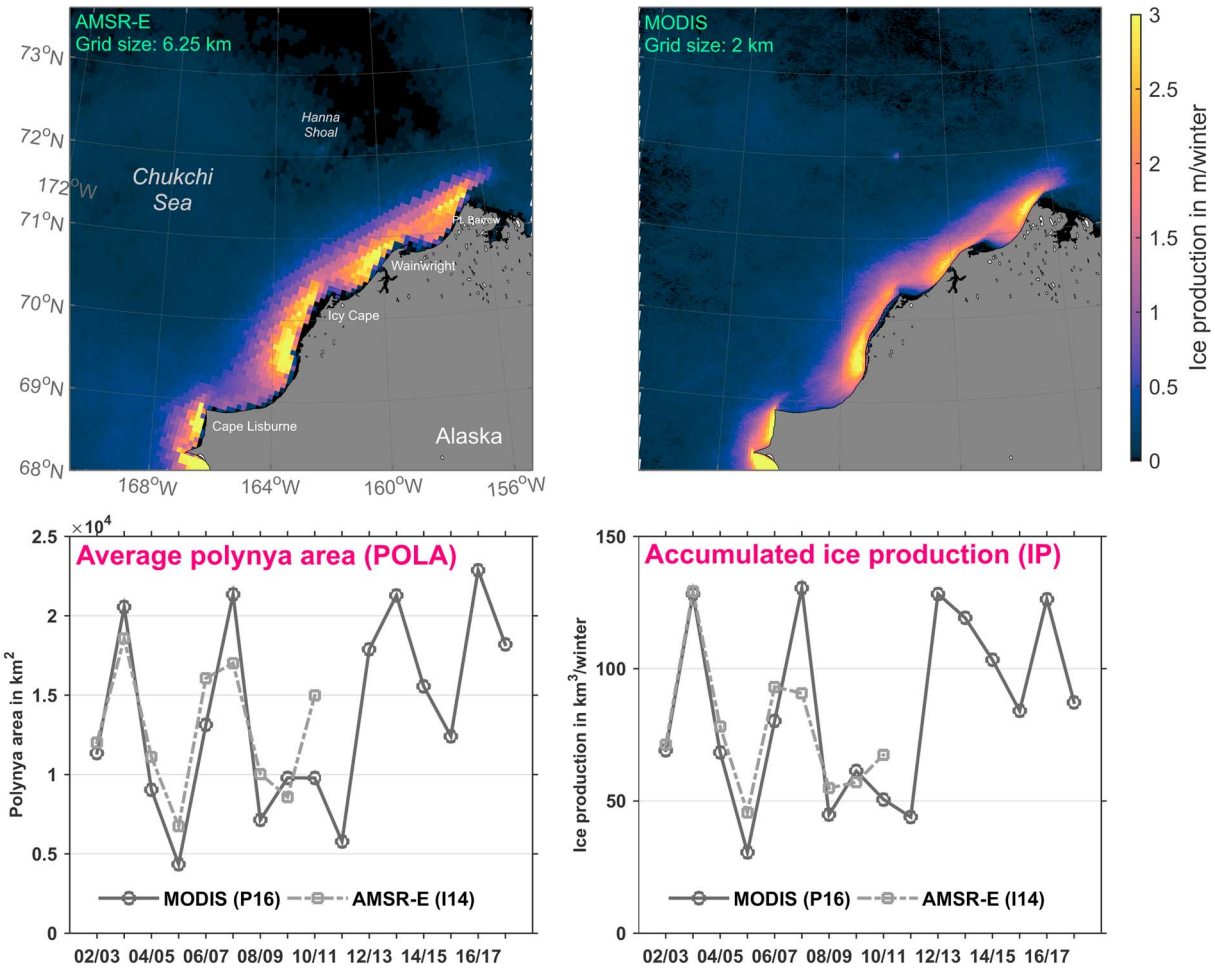

Figure 9. Comparison of Chukchi Sea polynya characteristics between the cloud-corrected MODIS data set (P16) and the AMSR-E data set (I14). The two upper panels show spatial distributions of the average (2002/2003 to 2010/2011) accumulated ice production (meters per winter) during winter (December to March) for each sensor. The lower left and right panels illustrate a time series of the annual average polynya area (POLA; TIT ≤ 0.2 m) in square kilometers and the annual accumulated ice production (IP) in cubic kilometers, respectively, from 2002/2003 to 2017/2018. Both sensor systems (MODIS/AMSR-E) are compared, where dark and light grey lines denote MODIS (P16) and AMSR-E (I14), respectively. MODIS = Moderate Resolution Imaging Spectroradiometer; AMSR-E = Advanced Microwave Scanning Radiometer-EOS; TIT = thin-ice thickness.

various others). Regular forming coastal polynyas appear along the Alaskan coastline due to strong offshore winds from northerly to easterly directions, most frequently around Point Barrow in the north over to Wainwright and Icy Cape down to Cape Lisburne in the south. Those polynyas are known for high wintertime IP (Cavalieri & Martin, 1994; Iwamoto et al., 2014; Tamura & Ohshima, 2011) and the resulting supply of cold and saline waters to the Alaskan Coastal Current, thereby contributing to maintaining the Arctic halocline layer (Cavalieri & Martin, 1994; Weingartner et al., 1998). However, previous remote sensing studies were mainly based on coarse resolution data with previously indicated limitations. While higher resolving thermal infrared data has been used by Preußer et al. (2016) in the past, their study had larger coverage gaps in the Chukchi Sea due to changes in cloud-detection (cf. Figure 3) which led to an obvious underestimation of the potential thermodynamic IP.

In contrast, the change to MODIS C6 data now introduces an increased coverage of valid MODIS data in this region (cf. previous sections) which leads to noticeable improvements on derived polynya metrics. This can be seen in Figure 9 (equivalent to Figure 8), which features an overview on wintertime (DJFM) polynya characteristics in the Chukchi Sea. Spatial distributions of the average accumulated IP (in meters per winter; upper row) from both MODIS and AMSR-E are now showing a vastly increased overall agreement, with high productive regions exceeding 3 m per winter being well detected by both satellites. Differences now become more apparent at the eastern margins of the most prominent polynya locations, where MODIS is capable of

capturing a finer structure of "bands" with high IP as well as more confined wintertime fast-ice areas (areas of near-zero IP next to the coastline). Further, a thin-ice area appearing within the pack-ice at Hanna Shoal that is presumably related to bathymetric effects is better resolved by MODIS, with IPRs exceeding 1 m per winter on average.

The average POLA for each winter between 2002 and 2018 lies within the range of 0.4 to 2.3×10^4 km^2, with no significant trends (see Table 3). Accumulated IP ranges between 25 and 125 km^3 per winter, and likewise to POLA there are no significant trends. Supporting that finding, Hirano et al. (2018) also found an absence of any significant trend or transition in the magnitude of IP between 1992 and 2014, and postulated that the year-to-year variability in IP is related to varying winter northeasterly wind stress. Derived metrics from AMSR-E and MODIS agree very well, with only 4% to 8% difference for both POLA and IP (Tables 3 and 4). Please note that neither I14/P16 nor this study considers a potential episodic suppression of thermodynamic sea IP through the hybrid latent/sensible heat mechanism in the northeastern part of the Chukchi Sea, which originates from a combination of wind-driven sea ice divergence and an upwelling of warmer waters (Hirano et al., 2016, 2018). Still, the improved agreement between both sensors in this highly dynamic polynya region greatly enhances the reliability of both approaches and almost demands for more detailed high-resolution studies in this region.

4.3. Polynyas in the Canadian Arctic Archipelago

The importance of widely distributed polynyas in the Canadian Arctic has been known since several decades, with comprehensive investigations and overviews by Stirling (1980) and Stirling and Cleator (1981) dating back to the beginning of the 1980s and earlier. In a geographical sense, the CAA is a complex system of islands and channels in the northern part of Canada, where it faces the Arctic Ocean to the north and west. In the east, the CAA is bounded by Baffin Bay and northern Greenland, which frame the North Water polynya (Barber et al., 2001; Deming et al., 2002; Steffen, 1985, 1986; Preußer et al., 2015, and others) at the the southern end of Nares Strait (cf. Figure 1). Hannah et al. (2009) presented an updated overview on known polynyas in the CAA (based on Barber & Massom, 2007; Stirling & Cleator, 1981), and introduced metrics to investigate the influence of tidal currents on polynyas in the archipelago. They noted that the dynamics of many of these recurring polynyas are to a large degree influenced by tidal currents, promoting a potential sensible heat influence on polynya formation and/or maintenance that would lower our calculated potential heat loss to the atmosphere through an oceanic component in the surface energy balance equation. Related processes were also documented by Melling et al. (2015). Similar to earlier mapping efforts, Tamura and Ohshima (2011) and Iwamoto et al. (2014) used passive microwave data for a coarse resolution inventory of polynyas in the Canadian Arctic with inherent underestimations of the small scale polynyas and flaw/shore leads that are frequently occurring in that region.

Hence, Figure 10 now shows the direct comparison (equivalent to Figures 8 and 9) between the average accumulated IP from AMSR-E and MODIS data (upper row). In case of the CAA, differences in the spatial distribution of polynyas become more apparent than in other regions of the Arctic. While core polynya areas with (very) high IP values in the eastern part of the CAA are more or less equally well detected (e.g., eastern exit of Jones Sound with around 10 m per winter; some detail in high IP areas hidden due to colorbar-scale), there are several areas with low to moderate IP in the central part of the CAA that are either exclusively visible in the MODIS data set, or more pronounced. These include polynyas and shore leads around Banks Island, south of Bathurst Island, east of Somerset Island, the shore areas of Lancaster Sound, northeast of Axel Heiberg Island, the northern exit region of McClure Strait, and the shore lead region east of Boothia peninsula. Note that some of these areas were not included in previous inventories such as Stirling and Cleator (1981) or Barber and Massom (2007), suggesting some alterations to the spatial distribution of polynyas in the CAA over the last years, or potential shifts in the timing of polynya openings from spring toward the DJFM period. Differences between MODIS and AMSR-E regarding the spatial distribution of IP become further apparent in the long term time series of the average wintertime POLA (in square kilometers) and wintertime accumulated IP (in cubic kilometers), where the estimates from MODIS exceed those from AMSR-E every winter season. The average difference between MODIS and AMSR-E amounts to −46% (-7.9×10^3 km^2) in terms of POLA and −39% (−49 km^3) in terms of IP (Tables 3 and 4). The average IP from MODIS within the margins of the CAA (Figure 1; without the NOW polynya) amounts to about 129 ± 36 km^3 for the period 2002/2003 to 2017/2018 and shows a slight but nonsignificant positive tendency.

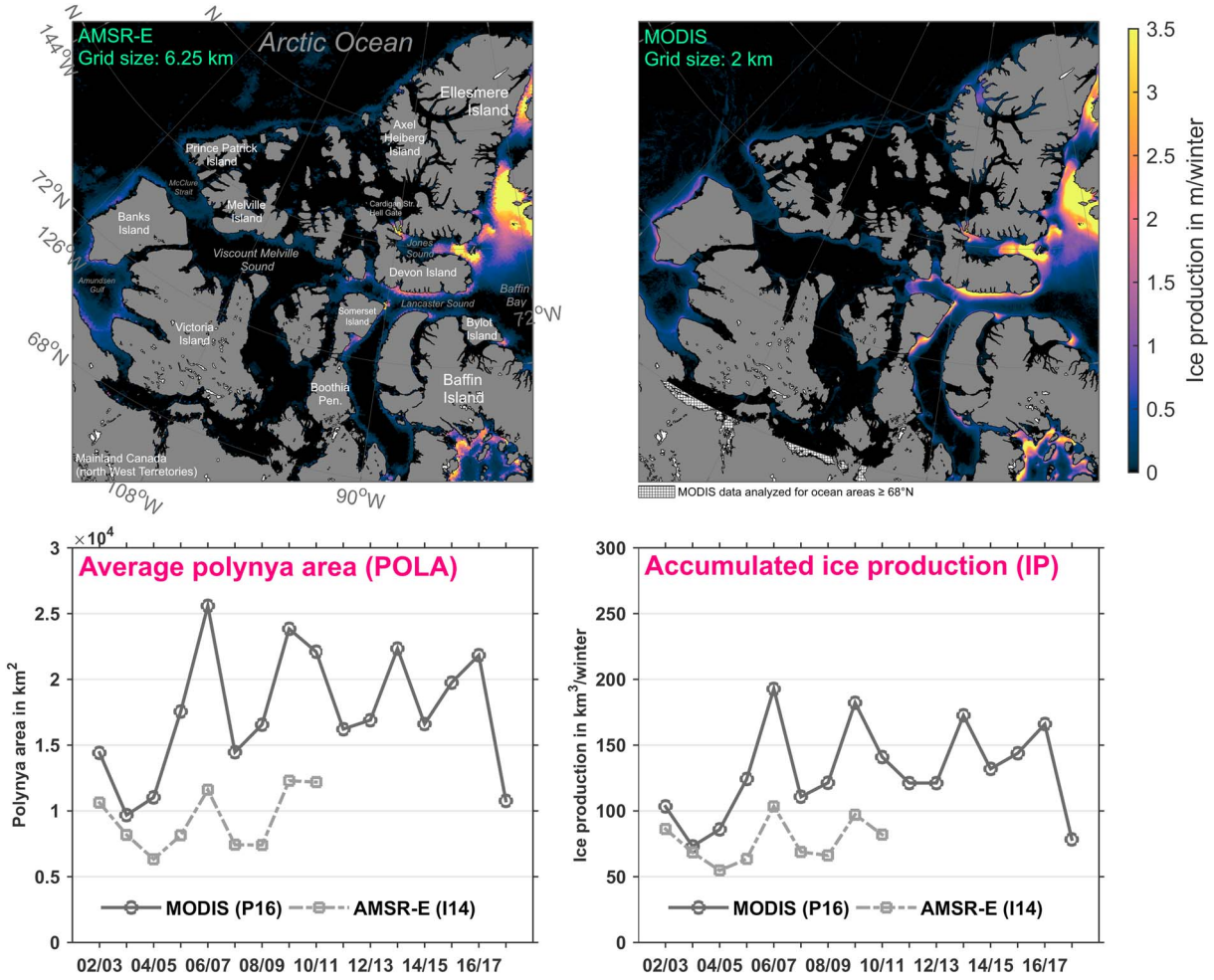

Figure 10. Comparison polynya characteristics in the Canadian Arctic Archipelago between the cloud-corrected MODIS data set (P16) and the AMSR-E data set (I14). The two upper panels show spatial distributions of the average (2002/2003 to 2010/2011) accumulated ice production (meters per winter) during winter (December to March) for each sensor. The lower left and right panels illustrate a time series of the annual average polynya area (POLA; TIT ≤ 0.2 m) in square kilometers and the annual accumulated ice production (IP) in cubic kilometers, respectively, from 2002/2003 to 2017/2018. Both sensor systems (MODIS/AMSR-E) are compared, where dark and light grey lines denote to MODIS (P16) and AMSR-E (I14), respectively. MODIS = Moderate Resolution Imaging Spectroradiometer; AMSR-E = Advanced Microwave Scanning Radiometer-EOS; TIT = thin-ice thickness.

The magnitude of average IP estimates from MODIS fit well to a statement by Agnew et al. (2008), who noted that the large number of stationary and transient wintertime polynyas and leads within the CAA are main contributors to the net sea ice fluxes into the Arctic Ocean and Baffin Bay, which combined amounts to a net loss of approximately 174 km^3 per year (2002 to 2007). While this value is small compared to other sea ice fluxes in the Arctic, it still underlines the importance of small polynyas and leads throughout the CAA and the need for high-resolution remote sensing data to monitor their wintertime dynamics.

5. Conclusions

Motivated by the high importance of thin-ice areas in the Arctic wintertime sea ice cover, this study presented a detailed comparison between two different and independently derived satellite data sets featuring TIT and IP estimates over 9 to 16 consecutive winter seasons. This is the first time that both passive microwave and purely thermal infrared approaches are directly compared to each other. However, before conducting this comparison, we first checked some on of the presumably most influential methodical differences such as cloud-effects (clear-sky bias/interpolation) as well as data version changes. The evaluation of clear-sky bias effects, originating from the circumstance that the MODIS thermal infrared (i.e., optical) sensors cannot penetrate clouds and thus only clear-sky pixels can be utilized to monitor processes at the surface, showed a rather low degree of overestimation of the heat loss. It showed that AMSR-E-based average

IP estimates in the Chukchi Sea are reduced by less than one standard deviation (or −0.7 cm/day on average) under cloudy conditions. Together with an estimated subdaily bias of 0.4 m/winter at maximum (Preußer et al., 2016), the total effect/overestimation can be as high as around 1 m/winter. It is regionally highly variable and might also be dependent on local weather conditions. As the AMSR-E approach is based on relating independently derived MODIS ice thicknesses to AMSR-E brightness temperatures, we also checked the possibility of an initial offset in ice thickness. It showed that this effect is of minor magnitude, with MODIS TIT from I14 being slightly higher than those in P16. However, this minor offset mostly affects TIT ≥ 20 cm (with higher uncertainties) and hence a thickness range that is neither analyzed in this study nor in most other polynya studies (such as I14 and P16).

Concerning the MODIS data set, the change from MxD29 C5 to C6 data introduced some noticeable changes of polynya statistics in many parts of the Arctic, which are overall considered to be an improvement on the data set in P16. The most pronounced changes are found in the Pacific sector (Chukchi Sea and East Siberian Sea), where for instance IP is increased by 233% to 482%. Furthermore, the extension of the MODIS data set up to the winter season 2017/2018 certainly enables a better evaluation of potential trends in POLA/IP for a rapidly changing Arctic Ocean after the year 2000 and onward than the current version of the AMSR-E data set which is only available until 2010/2011. A follow-up data set that extends this record using AMSR2 data is currently under development. As could be shown in this study, previously observed positive trends in IP (Preußer et al., 2016) on the Siberian shelf seas are also found in the 16-year data set, which underlines an apparent change in polynya dynamics in the Eastern Arctic and, connected to that, changing Transpolar Drift characteristics (Krumpen et al., 2019).

The direct comparison of the AMSR-E data set by Iwamoto et al. (2014) and the MODIS (C6) data set revealed an overall high agreement in both polynya extent (POLA) and IP (IP). The average POLA (average accumulated IP), all Arctic polynya regions (Figure 1) combined, is estimated with 1.99×10^5 km^2 (1.34×10^3 km^3) in case of MODIS and 2.29×10^5 km^2 (1.31×10^3 km^3) for AMSR-E during the overlapping period from 2002/2003 to 2010/2011. This corresponds to a relative difference of 15% in POLA and −2% in IP. Hence, we assume that sensor-specific strengths and weaknesses in each data set roughly counterbalance each other, as they become more or less apparent depending on the regarded region. As an example in the CAA, our study demonstrates a main advantage of the high-resolution MODIS data set, when larger leads/smaller polynyas within its narrow fjords and complex coastline can be resolved more frequently or even exclusively. However, it has to be noted that smaller and short-lived leads throughout the Arctic sea ice cover are still not well represented in this data set due to the cloud/data gap treatment and a strict persistence filtering. More research is necessary in order to be able to adequately address the proportion of leads that is only captured by dedicated MODIS lead retrievals (Willmes & Heinemann, 2016) and (quantifying) their role in ice formation processes. Aside from that, other prominent polynya regions such as the Laptev Sea or Chukchi Sea show only minor differences overall which further demonstrates that both data sets are able to capture the long-term dynamics of polynya occurrences and heat loss/ice growth.

Quite generally, we can say that the good agreement greatly enhances the reliability of the both data sets for monitoring and quantifying the ongoing changes in Arctic polynyas in the context of climatic changes as they were derived independent from each other. However and unfortunately, a continuous/seamless and updated passive microwave data set is currently only available for Antarctica (AMSR-E, SSM/I-SSMIS, AMSR2 -Nihashi et al., 2017) which prohibits a comparison for the most recent winter seasons. A similar future extension for the Arctic would be ideal to further complement the growing MODIS time series or even lead to a synthesis of both products. The latter would then need to address certain aspects/weaknesses that are currently considered to be the main areas of future improvement. Besides the above mentioned aspect concerning lead detection, these include for instance a re-evaluation of the empirical equations by Iwamoto et al. (2014; taking into account the knowledge of the small but existing offset to the MODIS data in this study) as well as advancements in terms of ice-type detection (Nakata et al., 2019). Further, as the thermal infrared approach to derive ice thickness estimates is in principal independent of the (thermal) sensor, the usage of other sensors such as the Sea and Land Surface Temperature Radiometer (SLSTR) on board Sentinel-3 (European Space Agency) is a feasible option (with individual adjustments and validation) to ensure the future continuation of a high-resolution polynya time series. Lastly, it would certainly be worth addressing the high sensitivity of calculated atmospheric heat fluxes to the variety of atmospheric reanalysis data sets (with variable resolutions, sea ice representation, etc.), which should benefit from incorporating data from higher resolving regional atmospheric models.

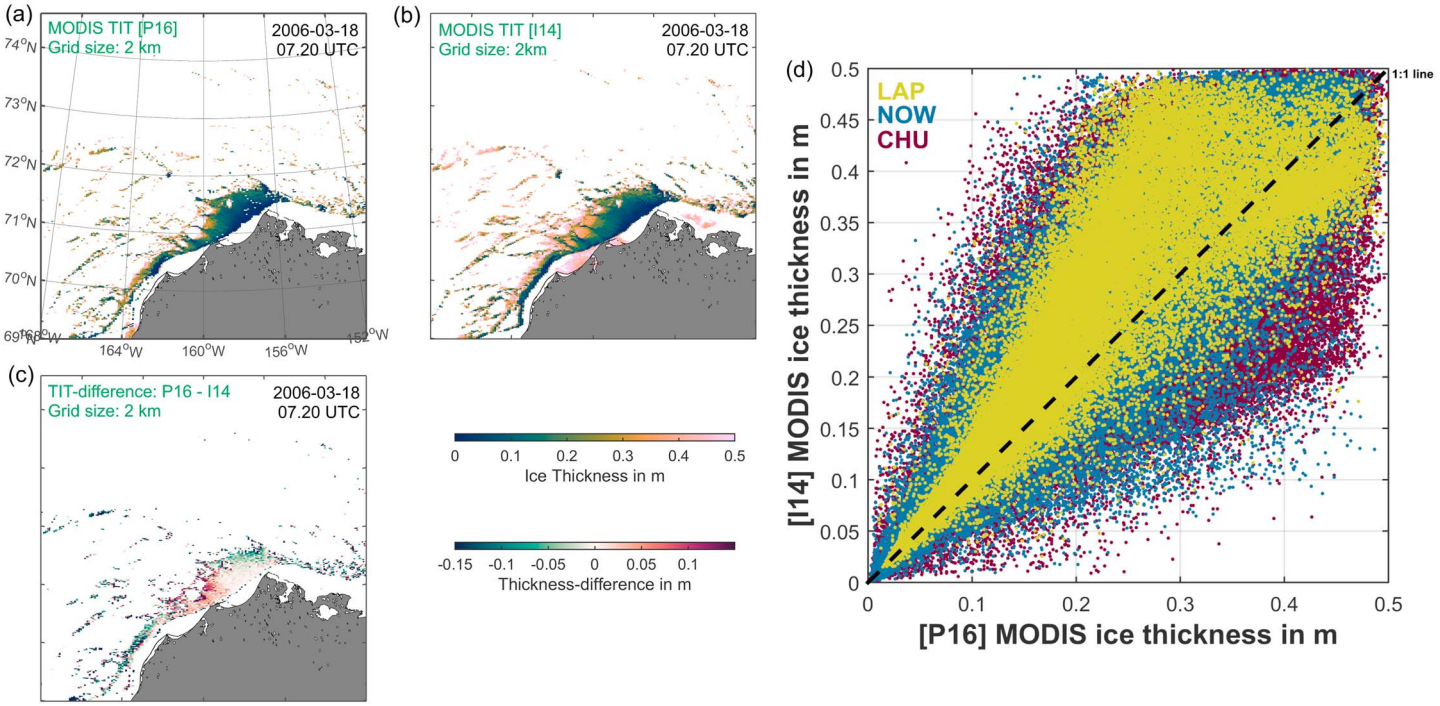

Figure A1. A case study (18 March 2006, 07.20 UTC) in panels (a) and (b) shows the spatial distribution of MODIS TIT up to 50 cm in the Chukchi Sea, calculated following Preußer et al. (2016; P16) and calculated by Iwamoto et al. (2014; I14), respectively. (c) The resulting difference in centimeters is presented, with positive values in reddish colors and negative values in green-blueish colors. (d) The scatterplot for all 16 case studies, originating from the Laptev Sea (LAP; 2 scenes), the North Water polynya (NOW; 3 scenes), and the Chukchi Sea (CHU; 11 scenes). Calculated thickness values from P16 (*x* axis) are compared to respective values from I14 (*y* axis). The 1:1 line is drawn as a dashed black line as a reference. MODIS = Moderate Resolution Imaging Spectroradiometer; TIT = thin-ice thickness.

Appendix A: Evaluation of Initial MODIS Offset

Section 2 indicated that the procedure to derive a thermal ice thickness from AMSR-E passive microwave data is based on empirically relating distinct ratios of microwave brightness temperatures to a certain set of hand-selected and mostly clear-sky MODIS IST swaths, from which reference ice thickness charts are calculated. Further, it was also mentioned that there are some differences in the procedure to derive MODIS thin-ice thicknesses between Iwamoto et al. (2014) and Preußer et al. (2016), possibly leading to an initial offset.

In order to evaluate the existence of such an offset, we selected the same 16 MODIS swaths with reference ice thicknesses that were being used in I14 (MODIS C5) and compared them directly to the corresponding charts from P16 (here: MODIS C6). All these MODIS swaths are taken from three different polynya regions:

Table A1
Comparison of MODIS (C6) Thin-Ice Thickness Data From P16 With Equivalent MODIS (C5) Thin-Ice Thicknesses Used by I14 as a Reference in Their AMSR-E Thin-Ice Thickness Algorithm

	Average TIT							
	LAP		NOW		CHU		Combined	
	(0 to 20 cm) (cm)	(20 to 50 cm) (cm)	(0 to 20 cm) (cm)	(20 to 50 cm) (cm)	(0 to 20 cm) (cm)	(20 to 50 cm) (cm)	(0 to 20 cm) (cm)	(20 to 50 cm) (cm)
[P16] MODIS thin-ice thickness	10.5 ± 4.5	32.2 ± 8.7	9.9 ± 5.1	33.0 ± 7.8	9.1 ± 5.4	33.9 ± 7.8	9.6 ± 5.1	33.5 ± 7.9
[I14] MODIS thin-ice thickness	11.6 ± 4.9	37.3 ± 7.6	10.6 ± 5.3	37.1 ± 7.9	9.8 ± 5.6	37.5 ± 8.2	10.4 ± 5.4	37.4 ± 8.1
BIAS (P16-I14)	−1.0 ± 2.6	−5.2 ± 9.3	−0.8 ± 4.0	−4.1 ± 7.9	−0.7 ± 3.8	−3.6 ± 9.0	−0.8 ± 3.6	−3.9 ± 8.8

Note. Averages (± standard deviation) for all case studies from the Laptev Sea (LAP), the North Water polynya (NOW), and Chukchi Sea (CHU) are given together with their combined average and standard deviation. In addition, the respective biases are indicated in the bottom row.

the North Water polynya (NW-Greenland/Smith Sound), the Laptev Sea polynyas (Russia), and the Chukchi Sea polynya (Alaska/United States).

Figures A1a–A1c show one exemplary case study of derived thin-ice thicknesses in the Chukchi Sea on 18 March 2006 (0720 UTC). Note that in this case the range of thin-ice thicknesses goes up to 50 cm, which implies that also values with high uncertainties beyond 20 cm (Adams et al., 2013) are visible at the margins of the polynya. Consequently, this thickness range (20 to 50 cm) represents areas where the largest differences (subpanel c) between both MODIS estimates (a and b) occur, while areas below 20 cm ice thicknesses seem to match up better. Hence, the margins of the polynya are most affected.

For all three polynya regions, Figure A1d presents the calculated thickness values from P16 compared to their respective counterparts from I14. While there is a wide spread of deviations that increases with increasing ice thicknesses and uncertainties, the thickness range up to 20 cm mostly follows the 1:1 line. However, a slight tendency toward thicker ice from I14 is visible. This tendency is confirmed in Table A1, which shows average ice thicknesses from P16 and I14 for all single case study regions together with their combined average and standard deviation. Resulting biases are further indicated in the bottom row. Overall, MODIS ice thicknesses by I14 are about 0.8 cm (for TIT $\leq$ 20 cm) and 3.9 cm (for TIT between 20 and 50 cm) thicker than the equivalent estimates by P16. It is noted that the respective standard deviations of 3.6 and 8.8 cm are about 2 to 4 times as high as the respective average value.

Acknowledgments
The National Snow and Ice Data Center (NSIDC) as well as the European Center for Medium-Range Weather Forecasts (ECMWF) are kindly acknowledged for providing the MODIS MxD29 sea ice product (https://n5eil01u.ecs.nsidc.org/) and the ERA-Interim atmospheric reanalysis data free of charge. The Ocean and Sea Ice dynamics group at the Institute of Low Temperature Science (Hokkaido University) provided the AMSR-E thin-ice thickness data set and ideal working conditions during a research stay of A. P. in 2016. This work was partly funded by Grant-in-Aids for Scientific Research (17H01157) of the Japanese Ministry of Education, Culture, Sports, Science and Technology (MEXT), the Japan Society for the Promotion of Science (JSPS), a research fund for Global Change Observation Mission Water 1 (GCOM-W1) of the Japan Aerospace Exploration Agency (JAXA) (PI ER2GWF404) and the Federal Ministry of Education and Research (Bundesministerium für Bildung und Forschung-BMBF) under Grant 03F0776D (The Changing Arctic Transpolar System—CATS). Supplementary data are available at the data repository PANGAEA (https://doi.pangaea.de/10.1594/PANGAEA.899854).

References

Ackerman, S., Frey, R., Strabala, K., Liu, Y., Gumley, L., Baum, B., & Menzel, P. (2010). Discriminating clear-sky from cloud with MODIS algorithm theoretical basis document (MOD35) version 6.1 (Tech. Rep.): MODIS Cloud Mask Team, Cooperative Institute for Meteorological Satellite Studies, University of Wisconsin.

Adams, S., Willmes, S., Schroeder, D., Heinemann, G., Bauer, M., & Krumpen, T. (2013). Improvement and sensitivity analysis of thermal thin-ice retrievals. *IEEE Transactions on Geoscience and Remote Sensing*, *51*(6), 3306–3318. https://doi.org/10.1109/tgrs.2012.2219539

Agnew, T., Lambe, A., & Long, D. (2008). Estimating sea ice area flux across the Canadian Arctic Archipelago using enhanced AMSR-E. *Journal of Geophysical Research*, *113*, C10011. https://doi.org/10.1029/2007JC004582

Aulicino, G., Fusco, G., Kern, S., & Budillon, G. (2014). Estimation of sea-ice thickness in Ross and Weddell Seas from SSM/I brightness temperatures. *IEEE Transactions on Geoscience and Remote Sensing*, *52*(7), 4122–4140. https://doi.org/10.1109/TGRS.2013.2279799

Barber, D. G., Hanesiak, J. M., Chan, W., & Piwowar, J. (2001). Sea-ice and meteorological conditions in northern Baffin Bay and the North Water polynya between 1979 and 1996. *Atmosphere-Ocean*, *39*(3), 343–359. https://doi.org/10.1080/07055900.2001.9649685

Barber, D. G., & Massom, R. A. (2007). The role of sea ice in Arctic and Antarctic polynyas. In W. O. Smith & D. G. Barber (Eds.), *Polynyas—Windows to the world* (pp. 1–54). Elsevier B.V., Amsterdam: Elsevier Oceanography Series. https://doi.org/10.1016/s0422-9894(06)74001-6

Bareiss, J., & Görgen, K. (2005). Spatial and temporal variability of sea ice in the Laptev Sea: Analyses and review of satellite passive-microwave data and model results, 1979 to 2002. *Global and Planetary Change*, *48*(1), 28–54. https://doi.org/10.1016/j.gloplacha.2004.12.004

Bauer, M., Schröder, D., Heinemann, G., Willmes, S., & Ebner, L. (2013). Quantifying polynya ice production in the Laptev Sea with the COSMO model. *Polar Research*, *32*(20922). https://doi.org/10.3402/polar.v32i0.20922

Cavalieri, D. J. (1994). A microwave technique for mapping thin sea ice. *Journal of Geophysical Research*, *99*, 12561. https://doi.org/10.1029/94jc00707

Cavalieri, D., Markus, T., & Comiso, J. (2004). AMSR-E/Aqua daily L3 12.5 km brightness temperature, sea ice concentration, and snow depth polar grids V002. Retrieved from https://nsidc.org/data/aesi12

Cavalieri, D. J., & Martin, Seelye (1994). The contribution of Alaskan, Siberian, and Canadian coastal polynyas to the cold halocline layer of the Arctic Ocean. *Journal of Geophysical Research*, *99*, 18343. https://doi.org/10.1029/94jc01169

Dee, D. P., Uppala, S. M., Simmons, A. J., Berrisford, P., Poli, P., Kobayashi, S., et al. (2011). The ERA-interim reanalysis: Configuration and performance of the data assimilation system. *Quarterly Journal of the Royal Meteorological Society*, *137*(656), 553–597. https://doi.org/10.1002/qj.828

Deming, JodyW, Fortier, Louis, & Fukuchi, Mitsuo (2002). The International North Water Polynya Study (NOW): A brief overview. *Deep Sea Research Part II: Topical Studies in Oceanography*, *49*(22-23), 4887–4892. https://doi.org/10.1016/s0967-0645(02)00168-6

Dethleff, D., Loewe, P., & Kleine, E. (1998). The Laptev Sea flaw lead—Detailed investigation on ice formation and export during 1991/1992 winter season. *Cold Regions Science and Technology*, *27*(3), 225–243. https://doi.org/10.1016/S0165-232X(98)00005-6

Dmitrenko, I. A., Kirillov, S. A., Tremblay, L. B., Bauch, D., & Willmes, S. (2009). Sea-ice production over the Laptev Sea shelf inferred from historical summer-to-winter hydrographic observations of 1960s–1990s. *Geophysical Research Letters*, *36*, L13605. https://doi.org/10.1029/2009GL038775

Dmitrenko, I. A., Tyshko, K. N., Kirillov, S. A., Eicken, H., Hölemann, J. A., & Kassens, H. (2005). Impact of flaw polynyas on the hydrography of the Laptev Sea. *Global and Planetary Change*, *48*(1), 9–27. https://doi.org/10.1016/j.gloplacha.2004.12.016

Drucker, R., Martin, S., & Moritz, R. (2003). Observations of ice thickness and frazil ice in the St. Lawrence Island polynya from satellite imagery, upward looking sonar, and salinity/temperature moorings. *Journal of Geophysical Research*, *108*(C5), 3149. https://doi.org/10.1029/2001jc001213

Ebner, L., Heinemann, G., Haid, V., & Timmermann, R. (2014). Katabatic winds and polynya dynamics at Coats Land, Antarctica. *Antarctic Science*, *26*(3), 309–326. https://doi.org/10.1017/S0954102013000679

Ebner, L., Schröder, D., & Heinemann, G. (2011). Impact of Laptev Sea flaw polynyas on the atmospheric boundary layer and ice production using idealized mesoscale simulations. *Polar Research*, *30*(7210), 16. https://doi.org/10.3402/polar.v30i0.7210

Ernsdorf, T., Schröder, D., Adams, S., Heinemann, G., Timmermann, R., & Danilov, S. (2011). Impact of atmospheric forcing data on simulations of the Laptev Sea polynya dynamics using the sea-ice ocean model FESOM. *Journal of Geophysical Research*, *116*, C12038. https://doi.org/10.1029/2010jc006725

Fukamachi, Y., Simizu, D., Ohshima, K. I., Eicken, H., Mahoney, A. R., Iwamoto, K., et al. (2017). Sea-ice thickness in the coastal northeastern Chukchi Sea from moored ice-profiling sonar. *Journal of glaciology*, *63*(241), 888–898. https://doi.org/10.1017/jog.2017.56

Gutjahr, O., & Heinemann, G. (2018). A model-based comparison of extreme winds in the Arctic and around Greenland. *International Journal of Climatology*, *38*(14), 5272–5292. https://doi.org/10.1002/joc.5729

Gutjahr, O., Heinemann, G., Preußer, A., Willmes, S., & Drüe, C. (2016). Quantification of ice production in Laptev Sea polynyas and its sensitivity to thin-ice parameterizations in a regional climate model. *The Cryosphere*, *10*(6), 2999–3019. https://doi.org/10.5194/tc-10-2999-2016

Hall, D. K., Key, J. R., Casey, K. A., Riggs, G. A., & Cavalieri, D. J. (2004). Sea ice surface temperature product from MODIS. *Geoscience and Remote Sensing, IEEE Transactions on*, *42*(5), 1076–1087. https://doi.org/10.1109/tgrs.2004.825587

Hannah, C. G., Dupont, F., & Dunphy, M. (2009). Polynyas and tidal currents in the Canadian Arctic Archipelago. *Arctic*, 83–95.

Heinemann, G. (2018). An aircraft-based study of strong gap flows in Nares Strait, Greenland. *Monthly Weather Review*, *146*(11), 3589–3604. https://doi.org/10.1175/MWR-D-18-0178.1

Heinemann, G., & Rose, L. (1990). Surface energy balance, parameterizations of boundary-layer heights and the application of resistance laws near an antarctic ice shelf ront. *Boundary-Layer Meteorology*, *51*(1-2), 123–158. https://doi.org/10.1007/bf00120464

Hirano, D., Fukamachi, Y., Ohshima, K. I., Watanabe, E., Mahoney, A. R., Eicken, H., et al. (2018). Winter water formation in coastal polynyas of the eastern Chukchi shelf: Pacific and Atlantic influences. *Journal of Geophysical Research: Oceans*, *123*, 5688–5705. https://doi.org/10.1029/2017JC013307

Hirano, D., Fukamachi, Y., Watanabe, E., Ohshima, K. I., Iwamoto, K., Mahoney, A. R., et al. (2016). A wind-driven, hybrid latent and sensible heat coastal polynya off Barrow, Alaska. *Journal of Geophysical Research: Oceans*, *121*, 980–997. https://doi.org/10.1002/2015JC011318

Hollands, T., & Dierking, W. (2016). Dynamics of the Terra Nova Bay polynya: The potential of multi-sensor satellite observations. *Remote Sensing of Environment*, *187*, 30–48. https://doi.org/10.1016/j.rse.2016.10.003

Itkin, P., & Krumpen, T. (2017). Winter sea ice export from the Laptev Sea preconditions the local summer sea ice cover and fast ice decay. *The Cryosphere*, *11*(5), 2383–2391. https://doi.org/10.5194/tc-11-2383-2017

Iwamoto, K., Ohshima, K. I., & Tamura, T. (2014). Improved mapping of sea ice production in the Arctic Ocean using AMSR-E thin ice thickness algorithm. *Journal of Geophysical Research: Oceans*, *119*, 3574–3594. https://doi.org/10.1002/2013jc009749

Iwamoto, K., Ohshima, K. I., Tamura, T., & Nihashi, S. (2013). Estimation of thin ice thickness from AMSR-E data in the Chukchi Sea. *International Journal of Remote Sensing*, *34*(2), 468–489. https://doi.org/10.1080/01431161.2012.712229

Jardon, F., Vivier, F., Bouruet-Aubertot, P., Lourenço, A., Cuypers, Y., & Willmes, S (2014). Ice production in Storfjorden (Svalbard) estimated from a model based on AMSR-E observations: Impact on water mass properties. *Journal of Geophysical Research: Oceans*, *119*, 377–393. https://doi.org/10.1002/2013JC009322

Kanamitsu, M., Ebisuzaki, W., Woollen, J., Yang, S.-K., Hnilo, J., Fiorino, M, & Potter, G. (2002). NCEP-DOE AMIP-II reanalysis (R-2). *Bulletin of the American Meteorological Society*, *83*(11), 1631–1643. https://doi.org/10.1175/BAMS-83-11-1631

König-Langlo, G., & Augstein, E. (1994). Parameterization of the downward long-wave radiation at the Earth's surface in polar regions. *Meteorologische Zeitschrift*, *N.F.3*(H.6), 343–347. https://doi.org/10013/epic.12338

Krumpen, T., Belter, H. J., Boetius, A., Damm, E., Haas, C., Hendricks, S., et al. (2019). Arctic warming interrupts the Transpolar Drift and affects long-range transport of sea ice and ice-rafted matter. *Scientific Reports*, *9*(1). https://doi.org/10.1038/s41598-019-41456-y

Krumpen, T., Janout, M., Hodges, K., Gerdes, R., Girard-Ardhuin, F., Hölemann, J., & Willmes, S. (2013). Variability and trends in Laptev Sea ice outflow between 1992–2011. *The Cryosphere*, *7*, 1–15. https://doi.org/10.5194/tc-7-349-2013

Launiainen, J., & Vihma, T. (1990). Derivation of turbulent surface fluxes—An iterative flux-profile method allowing arbitrary observing heights. *Environmental Software*, *5*(3), 113–124. https://doi.org/10.1016/0266-9838(90)90021-w

Mäkynen, M., & Karvonen, J. (2017). MODIS sea ice thickness and open water–sea ice charts over the Barents and Kara seas for development and validation of sea ice products from microwave sensor data. *Remote Sensing*, *9*(12). https://doi.org/10.3390/rs9121324

Martin, S., & Cavalieri, D. J. (1989). Contributions of the Siberian shelf polynyas to the Arctic Ocean intermediate and deep water. *Journal of Geophysical Research*, *94*, 12,725–12,738. https://doi.org/10.1029/JC094iC09p12725

Martin, S., Drucker, R., Kwok, R., & Holt, B. (2004). Estimation of the thin ice thickness and heat flux for the Chukchi Sea Alaskan coast polynya from Special Sensor Microwave/Imager data, 1990-2001. *Journal of Geophysical Research*, *109*, C10012. https://doi.org/10.1029/2004JC002428

Martin, S., Drucker, R., Kwok, R., & Holt, B. (2005). Improvements in the estimates of ice thickness and production in the Chukchi Sea polynyas derived from AMSR-E. *Geophysical Research Letters*, *32*, L05505. https://doi.org/10.1029/2004GL022013

Maykut, G. A., & Church, P. E. (1973). Radiation climate of Barrow Alaska,1962–66. *Journal of Applied Meteorology*, *12*(4), 620–628. https://doi.org/10.1175/1520-0450(1973)012h0620:RCOBAi2.0.CO;2

Melling, H., Haas, C., & Brossier, E. (2015). Invisible polynyas: Modulation of fast ice thickness by ocean heat flux on the Canadian polar shelf. *Journal of Geophysical Research: Oceans*, *120*, 777–795. https://doi.org/10.1002/2014jc010404

Moore, G. W. K., & Våge, K. (2018). Impact of model resolution on the representation of the air-sea interaction associated with the North Water polynya. *Quarterly Journal of the Royal Meteorological Society*, *144*(714), 1474–1489. https://doi.org/10.1002/qj.3295

Morales-Maqueda, M., Willmott, A. J., & Biggs, N. (2004). Polynya dynamics: A review of observations and modeling. *Reviews of Geophysics*, *42*, RG1004. https://doi.org/10.1029/2002rg000116

Nakata, K., Ohshima, K. I., & Nihashi, S. (2019). Estimation of thin-ice thickness and discrimination of ice type from AMSR-E passive microwave data. *IEEE Transactions on Geoscience and Remote Sensing*, *57*(1), 263–276. https://doi.org/10.1109/TGRS.2018.2853590

Naoki, K., Ukita, J., Nishio, F., Nakayama, M., Comiso, J. C., & Gasiewski, A. (2008). Thin sea ice thickness as inferred from passive microwave and in situ observations. *Journal of Geophysical Research*, *113*, C02S16. https://doi.org/10.1029/2007JC004270

Nielsen-Englyst, P., Høyer, J. L., Madsen, K. S., Dybkjær, G., Tonboe, R., & Alerskans, E. (2018). In situ observed relationships between skin temperatures and 2 m air temperatures in the Arctic. *The Cryosphere Discussions*, *2018*, 1–29. https://doi.org/10.5194/tc-2018-150

Nihashi, S., Ohshima, K. I., & Tamura, T. (2017). Sea-ice production in Antarctic coastal polynyas estimated from AMSR2 data and its validation using AMSR-E and SSM/I-SSMIS data. *IEEE Journal of Selected Topics in Applied Earth Observations and Remote Sensing*, *10*(9), 3912–3922. https://doi.org/10.1109/JSTARS.2017.2731995

Ohshima, K. I., Watanabe, T., & Nihashi, S. (2003). Surface heat budget of the Sea of Okhotsk during 1987–2001 and the role of sea ice on it. *Journal of the Meteorological Society of Japan. Ser. II*, *81*(4), 653–677. https://doi.org/10.2151/jmsj.81.653

Paul, S., Willmes, S., Gutjahr, O., Preußer, A., & Heinemann, G. (2015). Spatial feature reconstruction of cloud-covered areas in daily MODIS composites. *Remote Sensing*, *7*(5), 5042–5056. https://doi.org/10.3390/rs70505042

Paul, S., Willmes, S., & Heinemann, G. (2015). Long-term coastal-polynya dynamics in the southern Weddell Sea from MODIS thermal-infrared imagery. *The Cryosphere*, *9*, 2027–2041. https://doi.org/10.5194/tc-9-2027-2015

Preußer, A., Heinemann, G., Willmes, S., & Paul, S. (2015). Multi-decadal variability of polynya characteristics and ice production in the North Water polynya by means of passive microwave and thermal infrared satellite imagery. *Remote Sensing*, *7*(12), 15,844–15,867. https://doi.org/10.3390/rs71215807

Preußer, A., Heinemann, G., Willmes, S., & Paul, S. (2016). Circumpolar polynya regions and ice production in the Arctic: Results from MODIS thermal infrared imagery from 2002/2003 to 2014/2015 with a regional focus on the Laptev Sea. *The Cryosphere*, *10*(6), 3021–3042. https://doi.org/10.5194/tc-10-3021-2016

Preußer, A., Willmes, S., Heinemann, G., & Paul, S. (2015). Thin-ice dynamics and ice production in the Storfjorden polynya for winter seasons 2002/2003–2013/2014 using MODIS thermal infrared imagery. *The Cryosphere*, *9*(3), 1063–1073. https://doi.org/10.5194/tc-9-1063-2015

Renfrew, I. A., King, J. C., & Markus, T. (2002). Coastal polynyas in the southern Weddell Sea: Variability of the surface energy budget. *Journal of Geophysical Research*, *107*(C6), 3063. https://doi.org/10.1029/2000JC000720

Riggs, G., & Hall, D. K. (2015). *MODIS sea ice products user guide to collection 6 [Computer software manual]*. Boulder, CO 80309-0449 USA: University of Colorado.

Sansiviero, M., Maqueda, M. M., Fusco, G., Aulicino, G., Flocco, D., & Budillon, G. (2017). Modelling sea ice formation in the Terra Nova Bay polynya. *Journal of Marine Systems*, *166*, 4–25. https://doi.org/10.1016/j.jmarsys.2016.06.013

Scott, K. A., Buehner, M., & Carrieres, T. (2014). An assessment of sea-ice thickness along the Labrador Coast from AMSR-E and MODIS data for operational data assimilation. *IEEE Transactions on Geoscience and Remote Sensing*, *52*(5), 2726–2737. https://doi.org/10.1109/TGRS.2013.2265091

Smith, S. D., Muench, R. D., & Pease, C. H. (1990). Polynyas and leads: An overview of physical processes and environment. *Journal of Geophysical Research*, *95*, 9461–9479. https://doi.org/10.1029/jc095ic06p09461

Steffen, K. (1985). Warm water cells in the North Water, northern Baffin Bay during winter. *Journal of Geophysical Research*, *90*, 9129–9136. https://doi.org/10.1029/JC090iC05p09129

Steffen, K. (1986). Ice conditions of an Arctic polynya: North Water in winter. *Journal of Glaciology*, *32*(112), 383–390. https://doi.org/10.3189/S0022143000012089

Stirling, I. (1980). The biological importance of polynyas in the Canadian Arctic. *Arctic*, *33*, 303–315. https://doi.org/10.2307/40509029

Stirling, I., & Cleator, H. (1981). Polynyas in the Canadian Arctic, Canadian Wildlife Service, Occasional Paper (45), 73.

Stroeve, J., Markus, T., Boisvert, L., Miller, J, & Barrett, A (2014). Changes in Arctic melt season and implications for sea ice loss. *Geophysical Research Letters*, *41*, 1216–1225. https://doi.org/10.1002/2013GL058951

Tamura, T., & Ohshima, K. I. (2011). Mapping of sea ice production in the Arctic coastal polynyas. *Journal of Geophysical Research*, *116*, C07030. https://doi.org/10.1029/2010jc006586

Tamura, T., Ohshima, K. I., Markus, T., Cavalieri, D. J., Nihashi, S., & Hirasawa, N. (2007). Estimation of thin ice thickness and detection of fast ice from SSM/I data in the Antarctic Ocean. *Journal of Atmospheric and Oceanic Technology*, *24*(10), 1757–1772. https://doi.org/10.1175/jtech2113.1

Tamura, T., Ohshima, K. I., & Nihashi, S. (2008). Mapping of sea ice production for Antarctic coastal polynyas. *Geophysical Research Letters*, *35*, L07606. https://doi.org/10.1029/2007gl032903

Timco, G., & Frederking, R. (1996). A review of sea ice density. *Cold Regions Science and Technology*, *24*(1), 1–6. https://doi.org/10.1016/0165-232X(95)00007-X

WMO, W. M. O. (2014). WMO sea-ice nomenclature (Edition 1970-2014).

Weingartner, T. J., Cavalieri, D. J., Aagaard, K., & Sasaki, Y. (1998). Circulation, dense water formation, and outflow on the northeast Chukchi shelf. *Journal of Geophysical Research*, *103*, 7647–7661. https://doi.org/10.1029/98JC00374

Willmes, S., Adams, S., Schröder, D., & Heinemann, G. (2011). Spatio-temporal variability of polynya dynamics and ice production in the Laptev Sea between the winters of 1979/80 and 2007/08. *Polar Research*, *30 (5971)*, 16. https://doi.org/10.3402/polar.v30i0.5971

Willmes, S., & Heinemann, G. (2016). Sea-ice wintertime lead frequencies and regional characteristics in the Arctic, 2003–2015. *Remote Sensing*, *8*(1), 4. https://doi.org/10.3390/rs8010004

Willmes, S., Krumpen, T., Adams, S., Rabenstein, L., Haas, C., Hoelemann, J., et al. (2010). Cross-validation of polynya monitoring methods from multisensor satellite and airborne data: A case study for the Laptev Sea. *Canadian Journal of Remote Sensing*, *36*(S1), S196–S210. https://doi.org/10.5589/m10-012

Winsor, P., & Björk, G. (2000). Polynya activity in the Arctic Ocean from 1958 to 1997. *Journal of Geophysical Research*, *105*, 8789–8803. https://doi.org/10.1029/1999JC900305

Winsor, P., & Chapman, D. C. (2002). Distribution and interannual variability of dense water production from coastal polynyas on the Chukchi Shelf. *Journal of Geophysical Research*, *107*(C7), 3079. https://doi.org/10.1029/2001JC000984

Yao, T, & Tang, C. (2003). The formation and maintenance of the North Water polynya. *Atmosphere-Ocean*, *41*(3), 187–201. https://doi.org/10.3137/ao.410301

Yu, Y., & Lindsay, R. W. (2003). Comparison of thin ice thickness distributions derived from RADARSAT geophysical processor system and Advanced Very High Resolution Radiometer data sets. *Journal of Geophysical Research*, *108*(C12), 3387. https://doi.org/10.1029/2002jc001319

Yu, Y, & Rothrock, D. (1996). Thin ice thickness from satellite thermal imagery. *Journal of Geophysical Research*, *101*, 25,753–25,766. https://doi.org/10.1029/96JC02242